



HAL
open science

The MUSE Ultra Deep Field (MUDF) – III: Hubble Space Telescope WFC3 Grism Spectroscopy and Imaging

Mitchell Revalski, Marc Rafelski, Michele Fumagalli, Matteo Fossati, Norbert Pirzkal, Ben Sunnquist, Laura J. Prichard, Alaina Henry, Micaela Bagley, Rajeshwari Dutta, et al.

► To cite this version:

Mitchell Revalski, Marc Rafelski, Michele Fumagalli, Matteo Fossati, Norbert Pirzkal, et al.. The MUSE Ultra Deep Field (MUDF) – III: Hubble Space Telescope WFC3 Grism Spectroscopy and Imaging. *Astrophys.J.Suppl.*, 2023, 265 (2), pp.40. 10.3847/1538-4365/acb8ae . hal-04006156

HAL Id: hal-04006156

<https://hal.science/hal-04006156>

Submitted on 10 Jun 2023

HAL is a multi-disciplinary open access archive for the deposit and dissemination of scientific research documents, whether they are published or not. The documents may come from teaching and research institutions in France or abroad, or from public or private research centers.

L'archive ouverte pluridisciplinaire **HAL**, est destinée au dépôt et à la diffusion de documents scientifiques de niveau recherche, publiés ou non, émanant des établissements d'enseignement et de recherche français ou étrangers, des laboratoires publics ou privés.



The MUSE Ultra Deep Field (MUDF). III. Hubble Space Telescope WFC3 Grism Spectroscopy and Imaging

Mitchell Revalski¹ , Marc Rafelski^{1,2} , Michele Fumagalli^{3,4} , Matteo Fossati^{3,5} , Norbert Pirzkal¹ , Ben Sunnquist¹ , Laura J. Prichard¹ , Alaina Henry¹ , Micaela Bagley⁶ , Rajeshwari Dutta^{3,5} , Giulia Papini³ , Fabrizio Arrigoni Battaia⁷ , Valentina D'Odorico^{4,8,9} , Pratika Dayal¹⁰ , Vicente Estrada-Carpenter¹¹ , Emma K. Lofthouse³ , Elisabeta Lusso^{12,13} , Simon L. Morris¹⁴ , Kalina V. Nedkova² , Casey Papovich^{15,16} , and Celine Peroux^{17,18}

¹ Space Telescope Science Institute, 3700 San Martin Drive, Baltimore, MD 21218, USA; mrevalski@stsci.edu

² Department of Physics and Astronomy, Johns Hopkins University, Baltimore, MD 21218, USA

³ Dipartimento di Fisica G. Occhialini, Università degli Studi di Milano-Bicocca, Piazza della Scienza 3, I-20126 Milano, Italy

⁴ INAF—Osservatorio Astronomico di Trieste, via G.B. Tiepolo 11, I-34143 Trieste, Italy

⁵ INAF—Osservatorio Astronomico di Brera, via Bianchi 46, I-23087 Merate (LC), Italy

⁶ Department of Astronomy, The University of Texas at Austin, Austin, TX 78712, USA

⁷ Max-Planck-Institut für Astrophysik, Karl-Schwarzschild-Straße 1, D-85748 Garching bei München, Germany

⁸ Scuola Normale Superiore, Piazza dei Cavalieri 7, I-56126, Pisa, Italy

⁹ IFPU—Institute for Fundamental Physics of the Universe, via Beirut 2, I-34151 Trieste, Italy

¹⁰ Kapteyn Astronomical Institute, University of Groningen, P.O. Box 800, 9700 AV Groningen, The Netherlands

¹¹ Department of Astronomy & Physics, Saint Mary's University, 923 Robie Street, Halifax, NS, B3H 3C3, Canada

¹² Dipartimento di Fisica e Astronomia, Università di Firenze, via G. Sansone 1, I-50019 Sesto Fiorentino, Firenze, Italy

¹³ INAF—Osservatorio Astrofisico di Arcetri, Largo Enrico Fermi 5, I-50125 Firenze, Italy

¹⁴ Centre for Extragalactic Astronomy, Durham University, South Road, Durham DH1 3LE, UK

¹⁵ Department of Physics and Astronomy, Texas A&M University, College Station, TX, 77843-4242, USA

¹⁶ George P. and Cynthia Woods Mitchell Institute for Fundamental Physics and Astronomy, Texas A&M University, College Station, TX, 77843-4242, USA

¹⁷ European Southern Observatory, Karl-Schwarzschild-Straße 2, D-85748 Garching bei München, Germany

¹⁸ Aix Marseille Université, CNRS, LAM (Laboratoire d'Astrophysique de Marseille) UMR 7326, F-13388, Marseille, France

Received 2022 November 11; revised 2023 January 9; accepted 2023 February 1; published 2023 March 16

Abstract

We present extremely deep Hubble Space Telescope (HST) Wide Field Camera 3 (WFC3) observations of the MUSE Ultra Deep Field. This unique region of the sky contains two quasars at $z \approx 3.22$ that are separated by only ~ 500 kpc, providing a stereoscopic view of gas and galaxies in emission and absorption across ~ 10 billion years of cosmic time. We have obtained 90 orbits of HST WFC3 G141 near-infrared grism spectroscopy of this field in a single pointing, as well as 142 hr of optical spectroscopy with the Very Large Telescope Multi Unit Spectroscopic Explorer (MUSE). The WFC3 (F140W, F125W, and F336W) and archival WFPC2 (F702W and F450W) imaging provides five-filter photometry that we use to detect 3375 sources between $z \approx 0-6$, including 1536 objects in a deep central pointing with both spectroscopic and photometric coverage. The F140W and F336W mosaics reach exceptional depths of $m_{AB} \approx 28$ and 29, respectively, providing near-infrared and rest-frame ultraviolet information for 1580 sources, and we reach 5σ continuum detections for objects as faint as $m_{AB} \approx 27$ in the grism spectra. The extensive wavelength coverage of MUSE and WFC3 allows us to measure spectroscopic redshifts for 419 sources, down to galaxy stellar masses of $\log(M/M_{\odot}) \approx 7$ at $z \approx 1-2$. In this publication, we provide the calibrated HST data and source catalogs as High Level Science Products for use by the community, which includes photometry, morphology, and redshift measurements that enable a variety of studies aimed at advancing our models of galaxy formation and evolution in different environments.

Unified Astronomy Thesaurus concepts: [Astronomical techniques \(1684\)](#); [Observational cosmology \(1146\)](#); [High-redshift galaxies \(734\)](#); [Galaxy photometry \(611\)](#); [Galaxy abundances \(574\)](#); [Galaxy evolution \(594\)](#)

1. Introduction

1.1. Scientific Motivation

Understanding the connections between galaxies and their surrounding gaseous environments is fundamental to advancing our theoretical models of galaxy formation and evolution (Conselice 2014; Somerville & Dave 2015; Rahmati et al. 2016; Naab & Ostriker 2017; Peeples et al. 2019; Corlies et al. 2020; Oppenheimer et al. 2020; Lochhaas et al. 2021). Studying these relationships and their change over cosmic

time requires sensitive multiwavelength observations of galaxies and their surrounding gas over a large range in redshift (Chen et al. 2010; Rubin et al. 2018; Dutta et al. 2021). While high-mass galaxies produce the majority of the light that we observe, low-mass galaxies at the faint end of the luminosity function dominate the population. These numerous low-mass galaxies are expected to have a significant impact, as they ionize the gas surrounding them in the cosmic web, and enrich it with heavy elements produced by star formation (Bouwens et al. 2016; Dayal & Ferrara 2018; Maiolino & Mannucci 2019; Bacon et al. 2021; Atek et al. 2022).

This enriched gas comprises the intergalactic medium (IGM) and circumgalactic medium (CGM), which consists of diffuse, multiphase gas that lies within the virial radii of galaxies (Tumlinson et al. 2017). This tenuous reservoir plays a crucial



Original content from this work may be used under the terms of the [Creative Commons Attribution 4.0 licence](#). Any further distribution of this work must maintain attribution to the author(s) and the title of the work, journal citation and DOI.

role in regulating a galaxy’s supply of gas, as stellar-driven feedback deposits enriched material beyond the disk that can recycle through the galaxy on a variety of timescales (Fielding et al. 2017; Peroux & Howk 2020; Chadayammuri et al. 2022; Pandya et al. 2022; Péroux et al. 2022). However, studying the connections between low-mass galaxies and the CGM at high redshift is challenging because the gas structures are intrinsically faint. In addition, the multiphase nature of the gas can only be fully characterized by combining the results of sensitive emission and absorption line studies (e.g., Steidel et al. 2010; Crighton et al. 2011; Turner et al. 2014; Bielby et al. 2019; Lofthouse et al. 2020; Stott et al. 2020; Beckett et al. 2021; Cooper et al. 2021; Fossati et al. 2021; Zabl et al. 2021; Bacon et al. 2023).

These observational challenges have made the study of quasar fields particularly insightful because the quasar light is selectively absorbed by the IGM and CGM as it travels to the observer, which reveals the gas in and around galaxies that reside in field, cluster, and group environments (Bechtold 2001; Khare 2013; Chen et al. 2020; Dutta et al. 2020, 2021; Lofthouse et al. 2023). In the past, these studies were limited by the requirement that sources needed to be preselected for targeting with long-slit or fixed aperture multi-object spectroscopy, which can bias the galaxy sample. This can be overcome with integral field units (IFUs), which provide a spectrum for every spatial pixel within the field of view (FOV), or by employing slitless spectroscopy. Slitless grism observations avoid the aperture effects associated with long-slit observations, and provide spectroscopy with a high signal-to-noise ratio (S/N) of a field at the cost of spectral resolution. Specifically, the data are typically low dispersion ($\lambda/\delta\lambda \approx 100$) in order to disperse the full spectral traces of objects onto the detector, and can require advanced data-processing techniques to properly extract spectra for sources in crowded fields (Pirzkal et al. 2004, 2013, 2017; Momcheva et al. 2016; Brammer 2019).

These types of observations have typically been conducted from the ground in the optical (Smith 1975; MacAlpine et al. 1977; Schneider et al. 1999; Salzer et al. 2000, 2005) to avoid high nightsky background levels and contamination from telluric emission at longer wavelengths. However, investigations of optical emission lines at higher redshifts are possible from space using the near-infrared (NIR) capabilities of the Hubble Space Telescope (e.g., Atek et al. 2010, 2011; Brammer et al. 2012; Colbert et al. 2013; Schmidt et al. 2014; Momcheva et al. 2016; Estrada-Carpenter et al. 2019; Pharo et al. 2019, 2020; Bowman et al. 2021; Simons et al. 2021; Noirot et al. 2022; Papovich et al. 2022; Backhaus et al. 2023).

1.2. The MUSE Ultra Deep Field (MUDF)

We have undertaken an ultra-deep, NIR, optical, near-ultraviolet (NUV), and X-ray spectroscopic and imaging survey of the quasar field P2139-443, with the goal of investigating galaxy evolution in different environments. This field hosts two bright ($m_r \approx 17.9$ and 20.5) quasars at $z \approx 3.22$ that are separated by only $\sim 1'$ on the sky, corresponding to a physical separation of ~ 500 kpc at $z \approx 3$. These two quasars are identified as J214225.78-442018.3 (also known as Q2139-4434, and hereafter QSO-SE) at $z = 3.221 \pm 0.004$ and J214222.17-441929.8 (Q2139-4433, hereafter QSO-NW) at $z = 3.229 \pm 0.003$ (Lusso et al. 2019). With a third quasar at

nearly the same redshift (Q2138-4427, $z \approx 3.17$) and a separation of $\sim 8'$, this field is a rare quasar triplet system (Francis & Hewett 1993; D’Odorico et al. 2002). There is also a fourth quasar near QSO-SE, albeit at a lower redshift ($z \approx 1.298$), and together, these quasars probe various environments, such as a rich galaxy group at $z \approx 0.88$, an IGM filament at $z \approx 3.04$, and a candidate protocluster at $z \approx 3.22$ (Fossati et al. 2019).

Our current observations of the MUDF involve a six-prong strategy to cover submillimeter, NIR, optical, NUV, and X-ray wavelengths in emission and absorption from $z \sim 0-6$. These consist of imaging and spectroscopy with (1) the Hubble Space Telescope (HST) Wide Field Camera 3 (WFC3; Turner-Valle et al. 2004; Kimble et al. 2008; MacKenty et al. 2010) and Wide Field and Planetary Camera 2 (WFPC2; Holtzman et al. 1995a, 1995b), (2) the Very Large Telescope (VLT) Multi Unit Spectroscopic Explorer (MUSE; Bacon et al. 2010), (3) the High Acuity Wide field K-band Imager (HAWK-I; Pirard et al. 2004; Casali et al. 2006; Arsenault et al. 2008; Kissler-Patig et al. 2008; Paufigue et al. 2010; Siebenmorgen et al. 2011), (4) the VLT Ultraviolet and Visual Echelle Spectrograph (UVES; Dekker et al. 2000), (5) the X-ray Multi-Mirror Mission (XMM-Newton; Jansen et al. 2001; Struder et al. 2001), and (6) the Atacama Large Millimeter/submillimeter Array (ALMA; Wootten & Thompson 2009). The relatively small separation of the bright quasars aids in collecting these multiwavelength data sets, as the region of interest ($\approx 2' \times 2'$) fits almost entirely within a single FOV for most of the instruments.

The survey was launched with our large European Southern Observatory (ESO) program (ESO PID 1100.A-0528, PI: M. Fumagalli) using VLT MUSE to observe this region, which we have dubbed the MUSE Ultra Deep Field (MUDF). The observations were obtained between 2017 August 15 to 2022 June 2, and accumulated a total of ~ 142 hr of on-sky data. These optical IFU observations are complemented by high-resolution spectroscopy of the two quasars using UVES on the VLT (ESO PIDs 65.O-0299, 68.A-0216, 69.A-0204, and 102.A-0194), which provides absorption line spectroscopy of numerous structures between $z \approx 0-3$ that we will connect with the physical properties of galaxies observed in emission. The VLT MUSE and UVES observations are detailed further in Lusso et al. (2019) and Fossati et al. (2019), and here we focus on the recently acquired and archival HST observations.

By combining emission and absorption line spectroscopy with high spatial resolution imaging, our program is designed to connect the gas and galaxies observed in emission with the gas seen through absorption within field, group, and cluster environments. This will provide a more complete census of their physical properties and reveal the role of low-mass galaxies in enriching the gas. Specifically, we aim to characterize the gas kinematics, density, temperature, dust content, and metallicity, and reveal how these physical properties are shaped by different environments at various redshifts.

In this third paper, we expand our study of the MUDF to incorporate recently acquired HST observations, and provide the custom-calibrated data and source catalogs for use by the community. We describe the program design and acquisition of the HST observations in Section 2, and we detail our custom-calibration of the direct imaging in Section 3. In Section 4 we

describe our process for identifying sources in the images and measuring their photometric properties, and in Section 5 we describe our simulation-based methods for extracting the slitless grism spectroscopy. In Section 6 we discuss our morphology measurements, and in Section 7 we describe the High Level Science Products (HLSPs) that are publicly available through the Mikulski Archive for Space Telescopes (MAST) portal. Finally, in Section 8 we summarize the current status of the program and discuss our planned forthcoming studies. We adopt the AB magnitude system (m_{AB} , Oke & Gunn 1983) throughout this study, and assume a standard cosmology with $\Omega_M \approx 0.3$, $\Omega_\Lambda \approx 0.7$, and $h \approx 0.7$ (Planck Collaboration et al. 2020).

2. Observations

2.1. Program Overview

We first provide an overview of the HST observations in the MUDF, followed by a more detailed description of the program design and data acquisition. In the NIR, we have observed this field with WFC3/IR onboard HST, obtaining 90 orbits of G141 grism spectroscopy and F140W imaging (Program ID 15637, PI: M. Rafelski & M. Fumagalli), resulting in the deepest HST grism survey ever conducted for a single field. The direct imaging consists of observations through the F140W filter to identify sources in the dispersed grism images, as well as with the F125W filter to constrain their spectral slopes. In the optical, we take advantage of archival HST WFPC2 imaging through the F702W and F450W filters (Program ID 6631, PI: P. Francis), which provide useful constraints on the morphological and photometric properties of sources in the field. In the NUV, we have obtained eight orbits of HST WFC3/UVIS imaging using the F336W filter (Program ID 15968, PI: M. Fossati). These observations probe the rest-frame UV emission of galaxies, allowing us to accurately characterize their star formation histories. Together, the HST observations provide five-filter photometry (F140W, F125W, F702W, F450W, and F336W) over the majority of the field, and the wavelengths sampled by each filter are shown in Figure 1. Details of the observations are provided in Table 1, and their on-sky locations are shown by outlined regions in Figure 2.

2.2. Observational Setup

The 90 orbits of WFC3/IR G141 grism spectroscopy and F140W imaging observations (Program ID 15637, PI: M. Rafelski & M. Fumagalli) were obtained in Cycle 26 between 2019 August 10 and September 14, with four failed visits repeated in 2020 March and September. The program was designed with a standard image-grism-image exposure sequence for each orbit, which provides direct imaging in the F140W filter to identify the location of each object. This is required to measure the photometric and morphological properties of sources, and model how each object is dispersed across the detector during the grism observations so that exposures from different orbits can be aligned, and overlapping sources may be deblended during spectral extraction.

The observations were carried out at three fixed position angles (PAs) of $PA_{APER} = -150^\circ.3$, $-130^\circ.3$, and $-112^\circ.3$, with the relative separations of $\sim 20^\circ$ to ensure that overlapping sources at one PA are well separated at other PAs. There are also sources outside the direct-imaging FOV that are dispersed onto one side of the detector by the grism, so four orbits were

allocated to wider-field imaging with the F140W filter using SPARS25 and NSAMP of 14. This wider imaging, combined with the primary images taken with each grism observation, provides the exact location of all sources with grism spectroscopy. Accordingly, the high spatial resolution F140W imaging serves as the anchor for source detection and astrometric alignment of our other data sets in this field.

The observations were designed to maximize the depth of the grism spectroscopy in the central pointing by minimizing the background from zodiacal light and variable airglow from the He I $\lambda 10820$ Å geocoronal line. This was accomplished by scheduling the observations with a minimum HST Sun angle of 60° , and excluding dates with low Earth limb angles. In each orbit, a direct image was obtained, followed by six grism exposures that were split up in order to minimize persistence, followed by another direct image. The direct imaging employed SPARS10 with NSAMP of 10 to avoid saturating the quasars, resulting in exposure times of ~ 93 s. The grism exposures used SPARS25 with NSAMP of 14, resulting in exposure times of ~ 328 s. By bracketing the grism exposures with the direct images, we further reduced the effect of He I airglow on the observations. Finally, the exposures were dithered using an extended six-point dither pattern in order to maximize the spectral resolution of the grism observations, and to improve the direct image quality by fully sampling the instrumental point-spread function.

In addition to the HST WFC3/IR F140W imaging, we observed the field over a single-orbit with the F125W filter on 2020 March 23 to obtain photometry that better constrains the spectral slope of each object during extraction. This pointing is centered slightly to the north of the main F140W field, in order to fully capture objects that are dispersed onto the detector by the grism that lie outside the primary F140W field. We also pursued a complimentary program that obtained eight orbits of imaging with WFC3/UVIS using the F336W filter (Program ID 15968, PI: M. Fossati). These observations were gathered during two visits on 2020 May 5 and 2020 July 12, and are critical for accurately modeling the star formation histories of each galaxy. The F125W and F336W on-sky locations are shown by the orange and purple regions in Figure 2.

Finally, we take advantage of existing WFPC2 optical imaging through the F450W and F702W filters (Program ID 6631, PI: P. Francis, Francis et al. 2001, 2013) that were originally obtained to study galaxy clusters in the field, and which provide us with useful constraints on the optical properties of many galaxies. The field was observed with the F450W filter for eight orbits between 2000 August 31 and September 2, while the F702W observations encompass six orbits on 1999 August 23. The F450W and F702W observations are cospatial, as shown by the dashed blue and green regions in Figure 2. There are also cospatial observations through the F410M filter; however, this bandpass is fully encompassed by the much deeper F450W observations, so we do not use the F410M data.

3. Direct Imaging

3.1. Drizzling the F140W Master Reference Mosaic

We aim to recover the highest possible spatial resolution in the HST images, which requires optimally aligning and combining the exposures to account for undersampling of the CCD detectors. Specifically, the telescope provides higher

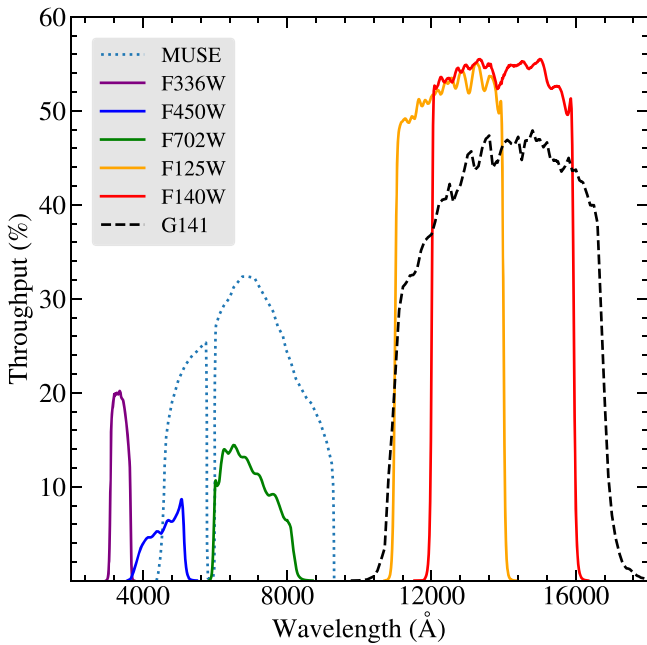


Figure 1. The total system throughputs for the HST WFC3 (F140W, F125W, and F336W) and WFPC2 (F702W and F450W) direct-imaging filters, as well as the WFC3 G141 grism, and VLT MUSE. The transmission curves include the quantum efficiency of the CCD detectors.

spatial resolution images than the detectors are able to record, which can be alleviated by making subpixel dithers between exposures. The maximum possible spatial resolution is then recovered by combining the images into a mosaic through a linear reconstruction process known as “drizzling” (Fruchter & Hook 2002). The Space Telescope Science Institute (STScI) provides a suite of tools for this within the DRIZZLEPAC¹⁹ software package (Gonzaga et al. 2012; Hoffmann et al. 2021).

First, a mosaic was produced by aligning and drizzling the HST WFC3/IR F140W images that were taken before and after each grism observation. The data were downloaded from the MAST archive on 2021 March 11, and were processed using the recently improved WFC3/IR Blob Flats (Olszewski & Mack 2021), and the most recent bad-pixel masks that were updated in the CDRS database²⁰ the day before. The 178 individual exposures were checked for quality, and 17 exposures with guiding or other issues were excluded. The remaining 161 exposures, each with an exposure time of ~ 93 s, were then aligned and drizzled using the TWEAKREG (v1.4.7) and ASTRODRIZZLE (v3.1.8) tools within DRIZZLEPAC (v3.1.8).

In order to align the exposures, we first ran the UPDATEWCS function with the USE_DB option set to False. This removes the default WCS coordinates that cause the direct images and grism exposures to be misaligned, and restores the most recent HST guide star based WCS coordinates. The images were then aligned to the Gaia EDR3²¹ (Prusti et al. 2016; Gaia Collaboration et al. 2021) astrometric coordinate system using TWEAKREG by creating a reference catalog of Gaia sources with position uncertainties of < 10 mas. We used the default TWEAKREG parameters, but we set the IMAGEFINDCFG THRESHOLD to 5σ and the PEAKMAX to 600 counts. There

were typically seven to nine bright sources meeting these criteria in each exposure, allowing the images to be aligned to within an rms error of only 16 mas (~ 0.12 native pixels).

This yielded an intermediate drizzle consisting of the F140W exposures directly associated with the grism observations, indicated by the solid red region in Figure 2. In addition, 28 longer exposures were obtained, split between four pointings (dashed red in Figure 2), to capture objects that are dispersed onto the detector by the grism and that lie outside of the primary F140W field. They have an exposure time of ~ 300 s each, and were individually aligned to the intermediate drizzle using TWEAKREG. The default parameters were used, except that sources in each exposure were identified with IMAGEFINDCFG values of CONV_WIDTH:3.5, THRESHOLD:4, and PEAKMAX:1000. The reference image parameters for REFIMAGEFINDCFG were set to CONV_WIDTH:5.0, THRESHOLD:6, and PEAKMAX:250. We employed the USE_SHARP_ROUND option to identify the cleanest sources, which yielded ~ 14 – 22 objects in each exposure. This process allowed us to align all of the F140W exposures to within an rms error of 21 mas (~ 0.16 native pixels).

These 189 exposures totaling 23,446 s (~ 6.5 hr) of on-sky time were then drizzled into a single master reference mosaic with a scale of $0''.06 \text{ pixel}^{-1}$. We optimized the ASTRODRIZZLE parameters to produce a mosaic with the fewest artifacts and maximum depth. One criterion is that the standard deviation of empty background regions in the weight (WHT) map, divided by the median value in that region, should be ≤ 0.2 (Section 6.3.3 of the DRIZZLEPAC Handbook v2.0; Hoffmann et al. 2021), which is controlled by varying the FINAL_PIXFRAC parameter. We also confirmed that the residual value in empty regions, which should be zero for a properly subtracted background, is $< 0.0002 \text{ counts s}^{-1}$. The adopted ASTRODRIZZLE parameters are listed in Table 2.

3.2. The F125W, F702W, F450W, and F336W Mosaics

We also produced drizzled images for the additional WFC3 and WFPC2 observations aligned to the F140W mosaic. The WFC3 F125W drizzle was produced using the same procedures as the F140W, except that the seven 303 s long exposures were aligned directly to the central F140W mosaic that is already astrometrically registered to Gaia. In the case of the WFPC2 F702W and F450W observations, we excluded short exposures with integration times of ≤ 120 s, as these would degrade the S/N of the drizzle. The F702W drizzle was produced in a similar manner as the other filters, with the exception that the background levels of the four individual detector chips were normalized to the median value of each exposure. This was accomplished by convolving each exposure by a Gaussian kernel with an FWHM of three pixels, masking all sources detected with $\geq 1\sigma$ certainty, and calculating the sigma-clipped median background value for all chips. The exposures were then individually equalized to their median values by subtracting the mean background of each chip from the median. The overall correction is small, with a typical dispersion for the individual chip background levels of ~ 0.4 – 0.8 counts. This correction was unimportant and not applied to the F450W filter, but for F702W, it yields a mosaic with a more uniform background, which is important for accurate photometry of a few objects that span multiple detector chips.

¹⁹ <https://www.stsci.edu/scientific-community/software/drizzlepac.html>

²⁰ <https://hst-crds.stsci.edu>

²¹ <https://www.cosmos.esa.int/web/gaia/early-data-release-3>

Table 1
Hubble Space Telescope Observations

Instrument and Camera	Filter or Grating	Effective Center λ (Å)	Zero-point (m_{AB})	Number of Orbits (N)	Exposure Time (s)	Image Depth ($5\sigma m_{AB}$)	Catalog Depth ($5\sigma m_{AB}$)	50% Complete Depth (m_{AB})	Image Area (arcmin ²)	PSF FWHM (")	Align rms (")	Sources Detected (N)
(1)	(2)	(3)	(4)	(5)	(6)	(7)	(8)	(9)	(10)	(11)	(12)	(13)
WFC3/IR	F140W	13,923	26.450	10	23,446	28.1	28.0	27.6	5.9	0.21	0.016	1422
	(deep)											
WFC3/IR	F140W	13,923	26.450	1	2100	27.5	27.2	27.0	17.9	0.21	0.021	1953
	(wide)											
WFC3/IR	F125W	12,486	26.232	1	2120	27.1	26.5	26.9	5.0	0.21	0.013	1248
WFPC2	F702W	6918	22.720	6	14,400	27.5	25.9	27.9	5.0	0.23	0.028	1168
WFPC2	F450W	4557	21.921	8	19,400	27.0	25.4	27.6	5.0	0.19	0.027	1092
WFC3/UVIS	F336W	3355	24.687	8	20,890	29.1	29.9	28.4	7.5	0.11	0.004	1580
WFC3/IR	G141	13,875	...	84	175,120	5.9	1499

Note. A summary of the HST observations for this field, with all images drizzled to a pixel scale of $0''.06 \text{ pixel}^{-1}$ (60 mas). The columns list (1) the HST instrument and camera, (2) the filter (imaging) or grating (spectroscopy), (3) the filter pivot wavelength, (4) the AB magnitude zero-point, (5) the effective number of orbits, (6) the exposure time in seconds, (7) the 5σ isophotal image depth measured from empty sky regions using an aperture of $0''.2$ in radius with uncertainties of ± 0.1 mag, (8) the 5σ isophotal depth measured for compact objects in the catalog with $S/N = 4.5\text{--}5.5$, (9) the 50% completeness depth (see Section 4.3), (10) the encompassed area on the sky, (11) the PSF FWHM, (12) the astrometric alignment rms error relative to Gaia (for the F140W) and relative to the F140W mosaic (all other filters), and (13) the number of detected sources. The orbital visibility differs for each observation, so an effective number of orbits is quoted for the imaging by assuming an average exposure time of 2400 s (40 minutes) per orbit. The F140W deep region includes the deep and wide exposures because they overlap spatially (see Figure 2). The G141 grism observations cover a spectral range of 10750–17000 Å ($\sim 1.1\text{--}1.7 \mu\text{m}$) with a resolving power of $R \approx 150$ at $1.4 \mu\text{m}$, where $R = \lambda/\delta\lambda$ and $\delta\lambda$ is equal to twice the dispersion. Finally, nonapplicable entries are indicated by ellipsis dots. These observations are available in MAST at doi:10.17909/q67p-ym16, together with our custom-calibrated data products at doi:10.17909/81fp-2g44 that can also be accessed from <https://archive.stsci.edu/hlsp/mudf>.

Finally, we applied several custom-calibrations to the WFC3/UVIS F336W exposures to use recent improvements. First, we used our publicly available codes^{22,23} that (1) flag negative divots adjacent to readout cosmic rays (ROCRs) in the data quality (DQ) arrays of each exposure that are otherwise overcorrected in the default pipeline, and (2) equalizes the background of the four amplifiers to remove background discontinuities, as discussed earlier for the WFPC2 F702W observations. These procedures are described in detail in Prichard et al. (2022; see their Section 2.2.2 and Appendix A), based on techniques from Rafelski et al. (2015).

Next, we corrected the F336W exposures for cosmic rays using our publicly available code²⁴ that is based on the Astropy implementation of the widely used LACOSMIC procedure (van Dokkum 2001; McCully et al. 2018; McCully & Tewes 2019). First, the procedure flags any negative pixels that are $> 5\sigma$ below the median background and replaces them with a random negative value drawn from the 1σ distribution. Without this correction, LACOSMIC improperly flags these $\sim 0.3\%$ of pixels as cosmic rays and replaces them with large groups of negative pixels. Next, LACOSMIC is run, and the procedure allows the user to detect cosmic rays in each exposure and either replace them with best-fitting values, or flag these as bad pixels in the data quality (DQ) arrays. We found that flagging the values in the DQ arrays so that they are ignored by ASTRODRIZZLE produces the cleanest drizzle for eight exposures. In cases with fewer exposures, the replacement method may be required. Using a conservative 6σ threshold, this process typically flags $\sim 5\%$ of the pixels as cosmic rays.

The exposures for each filter were then aligned to the F140W reference image using TWEAKREG, with alignment uncertainties $\sim 0.1\text{--}0.3$ native pixels (see Table 1). We used the same ASTRODRIZZLE parameters listed in Table 2 for all of the filters, except the FINAL_PIXFRAC was set to 0.7 for the F450W and F702W filters, and the COMBINE_TYPE was set to “minmed” for the F702W filter. The exposures in each filter were drizzled to produce mosaics at scales of $0''.06 \text{ pixel}^{-1}$, with additional properties summarized in Table 1.

3.3. Mosaic Postprocessing

Finally, we postprocessed the mosaics with our publicly available CREATE_NEG_RMS_IMAGES code²⁵ that generates a negative (NEG) image, and an rms error image from the weight map (WHT; in this case, the inverse variance map) of each mosaic, where $\text{rms} = 1/\sqrt{\text{WHT}}$. This postprocessing also replaces NaNs with zeros and infinite values with 1×10^{10} , which lie outside of the data region, but would otherwise cause issues in the analysis. We also corrected the rms maps for correlated pixel noise, which arises because the original pixels were shrunk to a smaller grid before drizzling, such that adjacent pixels share flux and noise information. If this effect is neglected, then the S/N will be overestimated when detecting and measuring the photometric and morphological properties of each object. The mathematical formalism is detailed in Section 3.3.2 of the DRIZZLEPAC Handbook (v2.0, Hoffmann et al. 2021), which provides a noise scaling factor (R) based on the drizzled and native pixel scales, and the FINAL_PIXFRAC used for each drizzle. Using our drizzle parameters, the noise scaling factors are $R = 1.733$ (F140W and F125W), $R = 1.629$ (F702W and F450W, neglecting the small planetary chip), and

²² https://github.com/lprichard/HST_FLC_corrections

²³ <https://github.com/bsunnquist/uvis-skydarks>

²⁴ https://github.com/mrevalski/hst_wfc3_lacosmic

²⁵ https://github.com/mrevalski/create_neg_rms_images

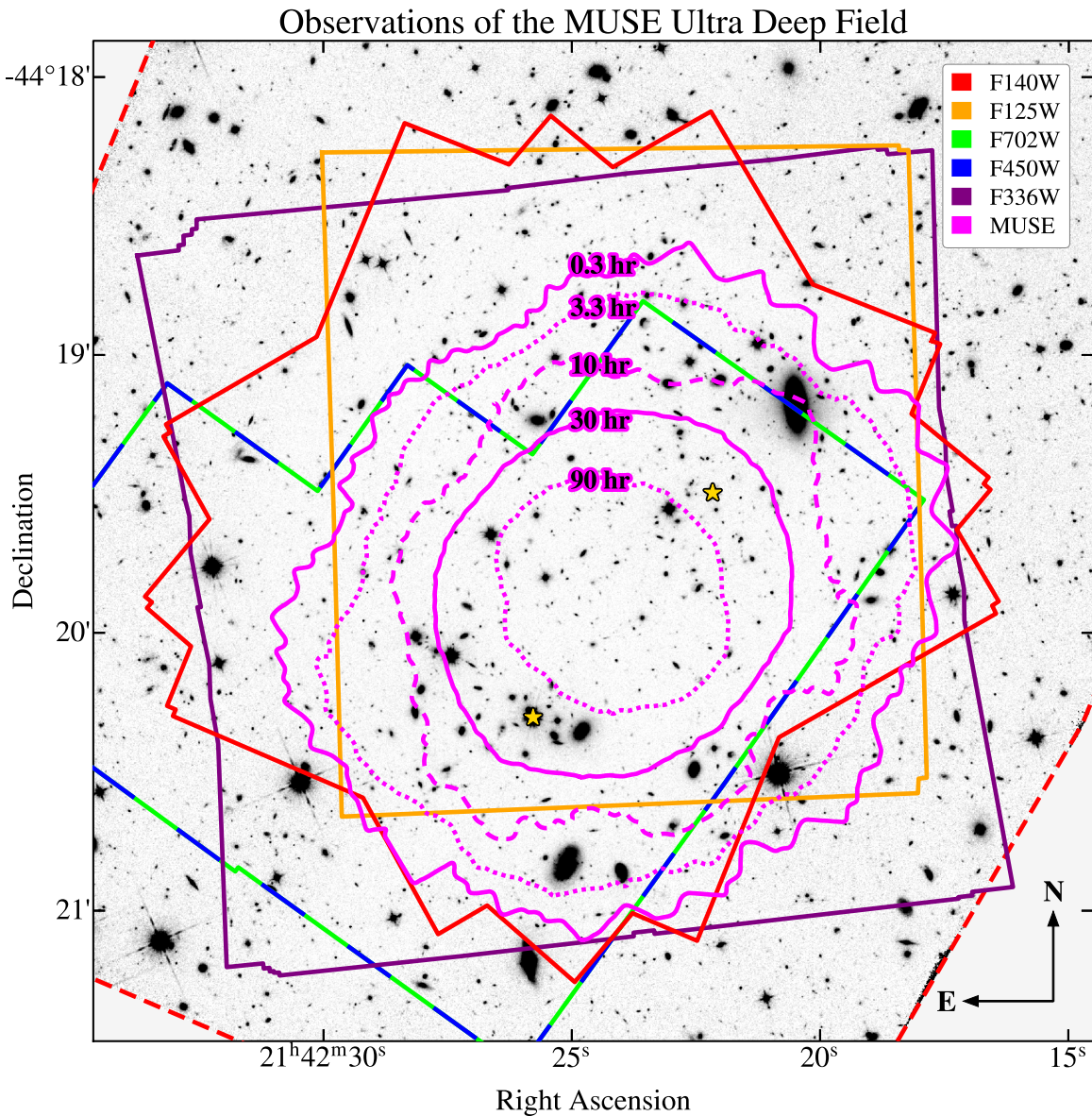


Figure 2. The region of the sky ($3\frac{1}{6} \times 3\frac{1}{6}$) containing the MUSE Ultra Deep Field, with instrument and filter coverage overlaid. The full field is covered by HST WFC3 F140W direct imaging, with a wide-shallow region (dashed red) and a narrow-deep region (solid red), with the data shown using a linear flux scaling. Additional HST WFC3 observations with the F125W (orange) and F336W (purple) filters are indicated by solid regions, as well as cospatial archival WFC2 observations with the F702W (dashed green) and F450W (dashed blue) filters. The depth of the MUSE observations is indicated by magenta contours that start at 90 hr and decrease by powers of three, with the centermost regions reaching a full depth of 120 hr. The locations of the two $z \approx 3.22$ quasars are indicated by gold stars, which are found within the 30 hr MUSE contour (solid magenta). Finally, the XMM-Newton and VLT HAWK-I observations cover areas larger than that shown in this graphic.

$R = 0.455$ (F336W). In the last case, the value is lower than unity because the drizzled pixel scale is larger than the native WFC3/UVIS pixel scale. Last, we visually inspected each drizzle, and for the F702W, F450W, and F336W mosaics, we used their weight maps to generate region files and mask the extreme edges of the data that contained noisy pixels. The F140W mosaic with these refinements serves as our reference image for source detection and the alignment of our other data sets in this field.

3.4. Point-spread Function Modeling

The spatial resolution of a telescope gradually decreases at longer wavelengths, which must be accounted for when measuring photometry in different filters. The spatial

resolution for each filter is characterized by its point-spread function (PSF), which is a measure of how an unresolved source is spread onto the detector after being distorted by the optical elements of the telescope and instrument. Using a model of the PSF for each filter, the spatial resolution of the images can be degraded to match that of the longest-wavelength image, which ensures that photometric measurements in different bandpasses sample the same intrinsic spatial area on the sky.

We used our publicly available code `HST_WFC3_PSF_MODELING`²⁶ to construct PSF models for each mosaic. This code uses our source catalog (Section 4) to identify bright,

²⁶ https://github.com/mrevalski/hst_wfc3_psf_modeling

Table 2
ASTRODRIZZLE Parameters

Parameter	Value
UPDATEWCS	False
STEPSIZE	1
SKYSUB	True
SKYMETHOD	globalmin+match
COMBINE_TYPE	imedian
FINAL_WHT_TYPE	IWM
FINAL_PIXFRAC	0.6
FINAL_UNITS	cps
FINAL_SCALE	0.06
FINAL_ROT	0.0

Note. The ASTRODRIZZLE parameters used to create the F140W mosaic (Section 3). These settings were also used for the other HST filters, except that the FINAL_PIXFRAC was set to 0.7 for the F702W and F450W filters, and the COMBINE_TYPE was set to “minmed” for the F702W filter.

isolated stars in each mosaic, and extracts a subimage of each star for stacking. The subimages are then normalized to their peak values and are interpolated to a finer grid for more precise alignment. The subimages are fit with Moffat profiles to determine the exact centroid location of each star, and they are then aligned to a common centroid. Finally, we calculate the mean and median of the aligned subimages, reinterpolate the results back to the mosaic pixel scale, and normalize the models to a total flux of unity. When a sufficiently large number of stars is available, adopting the median rather than the mean provides a higher S/N PSF model that robustly rejects contaminating sources.

In the case of the F140W and F125W images, nine stars²⁷ were used in the median model stack, and six of these same stars were available for the F702W and F450W filters. Finally, four of these stars were used in the F336W stack. While a larger number of stars is desirable, the alternative is to use synthetic empirical PSF models, which do not accurately capture the extended wings of the PSF at the present time. The resulting PSF models are $4'' \times 4'' \times 14$ (69×69 pixels) in size, and they are shown on logarithmic scales in Figure 3.

We used these PSF models to generate convolution kernels that match (degrade) the spatial resolution of each drizzle to the F140W reference mosaic, which ensures that the photometric measurements in each filter are comparable. We created the kernels using the PSF Matching feature within Astropy’s photutils (v0.7) software package, and adopted a standard Hanning window function, with the resulting convolution kernels shown in Figure 3. We then convolved the images with their respective kernels using the convolve feature within the SciPy (v1.3.1) multidimensional image processing (ndimage) - package. These PSF-matched mosaics are used for photometry with SOURCEEXTRACTOR (Section 4), while the unaltered mosaics are used for morphologies with STATMORPH (Section 6). In general, the differences for the photometry measured from the original and convolved images are negligible for bright sources, but become increasingly important for the faintest sources (e.g., for the F125W mosaic $\delta m \approx 0.1\text{--}0.3$ mag).

Table 3
SOURCEEXTRACTOR Parameters

Parameter	Deep Detection	Shallow Detection
DETECT_MINAREA	9 pixels	6 pixels
DETECT_THRESH	0.6σ	1.8σ
ANALYSIS_THRESH	0.6σ	1.8σ
DEBLEND_NTHRESH	32	32
DEBLEND_MINCONT	0.005	0.00001
FILTER_NAME	Gauss_3.0_5x5	Gauss_3.0_5x5
WEIGHT_TYPE	MAP_RMS	MAP_RMS
CLEAN_PARAM	5	5
Sources Extracted	3356	1722

Note. The SOURCEEXTRACTOR parameters used for all HST filters to create the MUDF catalog. The rms maps were corrected for correlated pixel noise (see Section 3.3), without which the equivalent deep and shallow thresholds are 1.1σ and 3.0σ , respectively. We conservatively set the F140W and F125W SEEING_FWHM parameter to $0''.16$ for maximum detections and used the PSF FWHM values listed in Table 1 for the remaining filters. The images are background subtracted, and so no background parameters were specified. The GAIN parameter was set to the exposure time for each filter (Table 1).

4. Source Catalog

4.1. Source Detection

The first step in analyzing the imaging, which is also required to extract the grism spectra, is to identify sources in the mosaics and measure their photometric and morphological properties. We selected SOURCEEXTRACTOR (v2.5.0; Bertin & Arnouts 1996) for this task, because it excels at detecting, segmenting, and deblending objects in crowded astronomical imaging. SOURCEEXTRACTOR creates a segmentation map by detecting a minimum number of adjacent pixels with fluxes above a user-defined threshold, determining which groups of pixels belong to unique sources based on a deblending scheme, and then assigning a common integer identification number to the pixels in each group representing a unique object. We constructed a segmentation map for the F140W image by running SOURCEEXTRACTOR with “deep” and “shallow” thresholds (also referred to as “hot” and “cold” in the literature) in order to better characterize the shapes and extents of faint and bright sources, respectively (see, e.g., Guo et al. 2013 and Rafelski et al. 2015 for in-depth discussions).

The deep threshold is intended to detect the faintest sources, and was determined by running SOURCEEXTRACTOR on the negative F140W image, which contains no true sources. The threshold is decreased incrementally, and the lowest value without false detections is adopted for the science image. The shallow threshold samples the brightest sources without encompassing nearby objects or extraneous background, and a value three times higher than the deep threshold was found to work well for this purpose. The final segmentation and photometry for each object is then selected from either the deep or shallow run based on a magnitude limit. In this way, bright sources are drawn from the shallow run, while faint sources are drawn from the deep run. A limit of $m_{F140W} = 19$ was experimentally determined so that the segmentation of each object best matches the extent of its emission in the imaging.

The deep and shallow segmentation maps and catalogs were then combined into single data products by taking objects brighter than $m_{F140W} = 19$ from the shallow run, replacing their

²⁷ Catalog IDs: 1246, 1535, 1983, 2003, 2210, 2291, 20493, 20723, 21182.

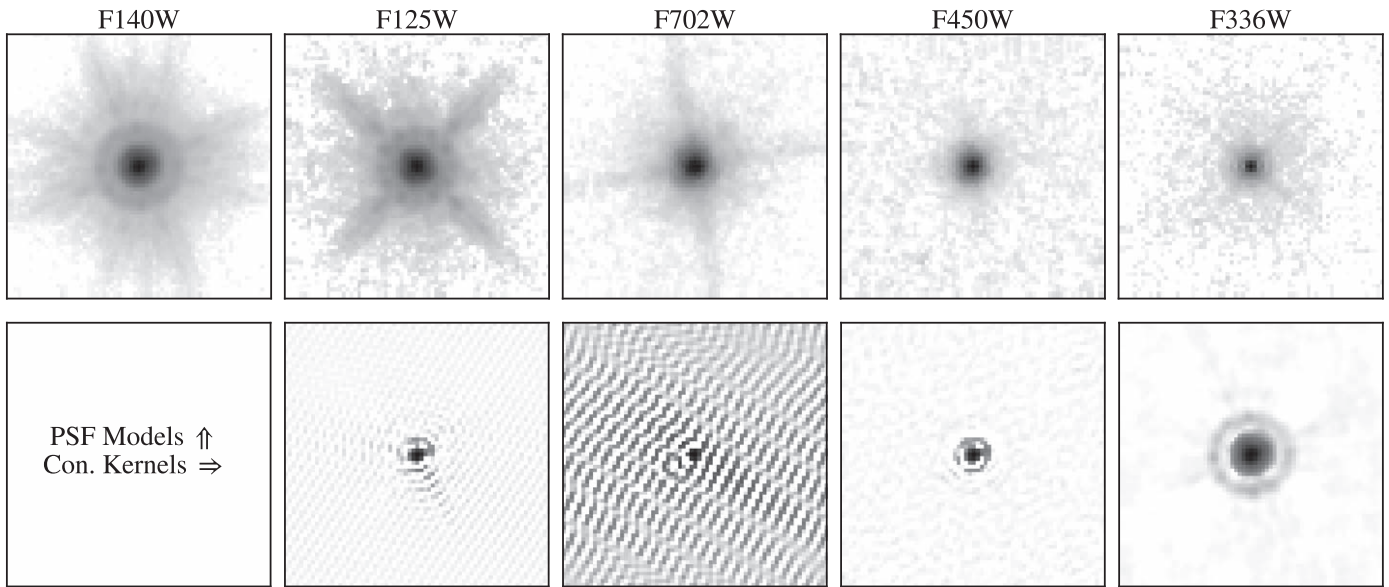


Figure 3. The WFC3 (F140W, F125W, and F336W) and WPC2 (F702W and F450W) PSF models (upper row) and convolution kernels (lower row) for the HST observations used in this study (see Table 1). The PSF models are displayed on logarithmic scales, with their total fluxes normalized to unity. The convolution kernels were generated using a standard Hanning window function, and are displayed on symmetrical logarithmic scales. As described in Section 3.4, the convolution kernels are used to create lower spatial resolution versions of each mosaic that match the F140W to ensure that the photometric measurements in each filter use equivalent apertures that sample the same area on the sky.

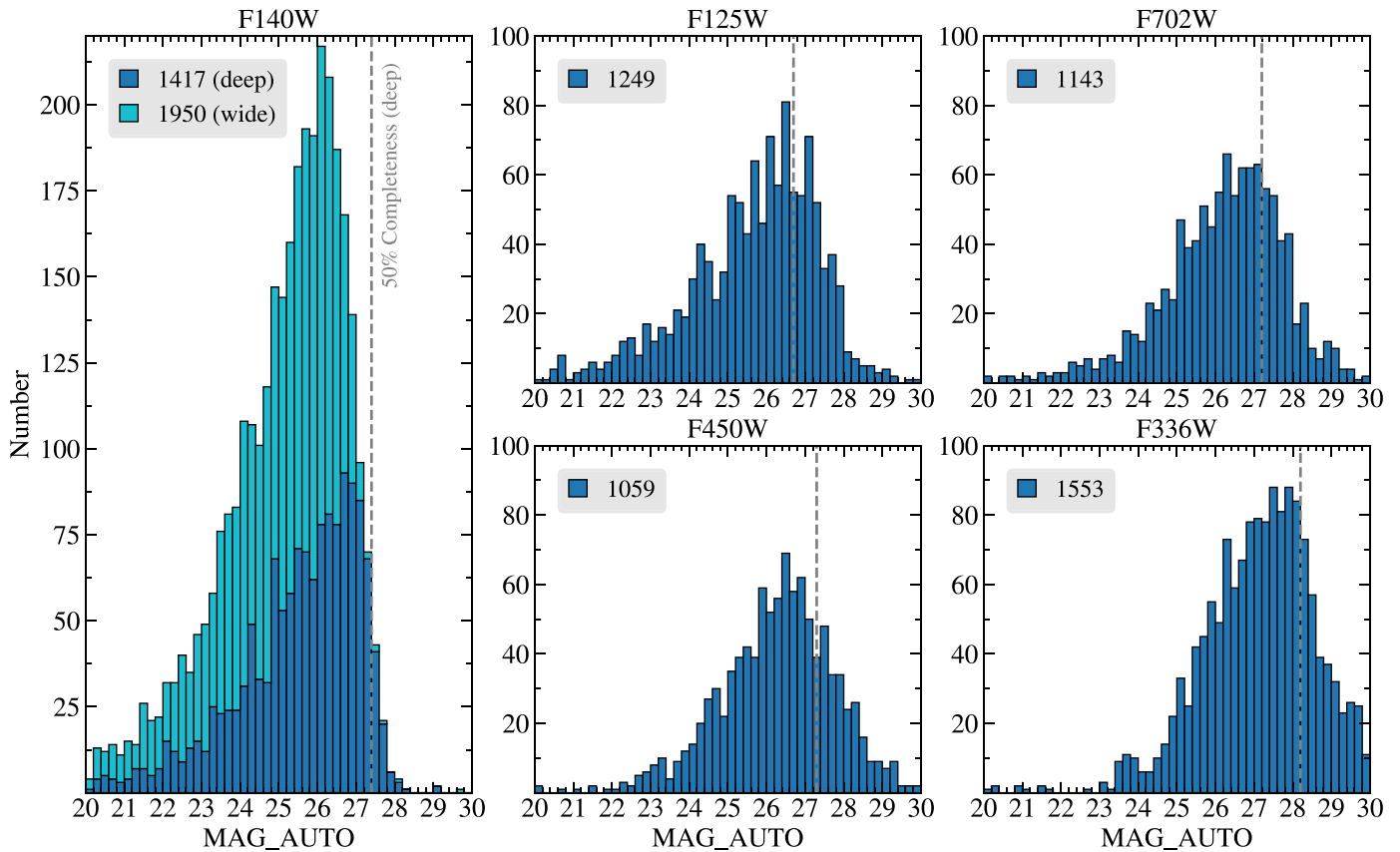


Figure 4. Histograms of the automatic magnitudes (MAG_AUTO) reported by SOURCEEXTRACTOR for real sources in each HST mosaic. The number of sources is listed in each legend, and all panels use 0.2 mag bin widths. Sources in the deep and wide regions of the F140W mosaic (see Figure 2) are stacked and are shown with blue and cyan, respectively. The brightest sources ($m_{AB} < 20$) are typically foreground stars, and the faintest sources ($m_{AB} > 30$) are noisy sources scattered above the detection threshold and so are not shown, and they are considered upper limits. The vertical dashed lines represent the depths at which the detection efficiency reaches 50% for unresolved sources, as shown in Figure 5.

Table 4
Source Catalog Columns

Column Number	SOURCEEXTRACTOR Parameter
(1)	NUMBER
(2)	X_IMAGE
(3)	Y_IMAGE
(4)	XMIN_IMAGE
(5)	YMIN_IMAGE
(6)	XMAX_IMAGE
(7)	YMAX_IMAGE
(8)	ALPHA_J2000
(9)	DELTA_J2000
(10)	A_IMAGE
(11)	B_IMAGE
(12)	THETA_IMAGE
(13)	ELONGATION
(14)	ELLIPTICITY
<hr/>	
(15)	KRON_RADIUS_F140W
(16)	FLUX_RADIUS_F140W
(17)	FWHM_IMAGE_F140W
(18)	CLASS_STAR_F140W
(19)	ISOAREA_IMAGE_F140W
(20)	MAG_ISO_F140W
(21)	MAGERR_ISO_F140W
(22)	FLUX_ISO_F140W
(23)	FLUXERR_ISO_F140W
(24)	MAG_AUTO_F140W
(25)	MAGERR_AUTO_F140W
(26)	FLUX_AUTO_F140W
(27)	FLUXERR_AUTO_F140W
(28)	BACKGROUND_F140W
(29)	FLAGS_F140W
<hr/>	
(30–44)	Same as Columns 15–29 for the F125W filter
(45–59)	Same as Columns 15–29 for the F702W filter
(60–74)	Same as Columns 15–29 for the F450W filter
(75–89)	Same as Columns 15–29 for the F336W filter
<hr/>	
(90)	SPEC_Z
(91)	SPEC_Z_ERR
(92)	SPEC_Z_FLAG

Note. The physical parameters included in the source catalog for the HST F140W, F125W, F702W, F450W, and F336W observations. The first seven columns provide the object ID number, the X and Y pixel locations, and their minimum and maximum extents. These are followed by the R.A. and decl., major and minor axis sizes, orientation angle, elongation, and ellipticity. There are then 15 columns that repeat for each filter, containing the various radii, magnitude, and flux measurements defined in SOURCEEXTRACTOR (<https://sextractor.readthedocs.io/en/latest/Measurements.html>). These include the isophotal (ISO) and aperture-corrected (AUTO) values. The last three columns provide the derived redshift, redshift uncertainty, and redshift quality flag. The source catalog is available in machine-readable form (see Section 7).

entries in the deep segmentation map and catalog with the corresponding shallow values, and adding +20,000 to the ID number²⁸ to indicate that these sources were drawn from the shallow run. The mosaic and merged segmentation map were then visually inspected to ensure that the segment for each object matched the physical extent of the source in the imaging, and five additional objects fainter than $m_{F140W} = 19$ were selected from the shallow run (IDs 588, 557, 780, 871, and 1182) for this same type of replacement. Finally, we manually

²⁸ The value of 20,000 is arbitrary, and any value higher than the number of sources in the deep run would suffice. In this case, there are $<10^4$ sources, so a value of $>10^4$ ensures an unambiguous identification for each source.

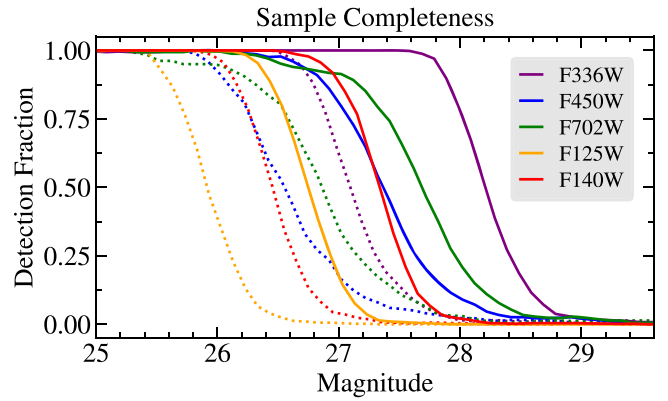


Figure 5. The fraction of artificial sources that are recovered in each mosaic as a function of magnitude for point sources (solid lines) and extended galaxies (dotted lines). The sources were injected at random locations, with limits to avoid the extreme edges of the mosaics, the locations of real sources in the segmentation map, and the locations of other injected sources. The adopted limiting magnitude is the value at which the detection fraction decreases to 50% (see Table 1).

reassigned the IDs of diffraction spikes to match their sources for 10 bright stars drawn from the shallow catalog, and included their fluxes and error budgets in the photometry for these stars. Ultimately, this process selected 103 sources from the shallow run and 3272 from the deep run for a total of 3375 sources. This procedure yields more reliable segmentation and photometry for very bright and faint sources than when using a single detection threshold, and the adopted SOURCEEXTRACTOR parameters are summarized in Table 3.

4.2. Photometric Catalog

The photometry for all filters was measured using SOURCEEXTRACTOR in dual-image mode, where sources are detected in the deep F140W reference image, and then their fluxes are measured in the mosaic for each filter. If an object is detected above the user-specified thresholds (see Table 3), then SOURCEEXTRACTOR measures the photometric parameters for that object. We used the same deep and shallow modes applied to the F140W, and the two catalogs for each filter were merged so that only the deep or shallow entry was adopted, matching the selection that was made for the F140W catalog.

The measured fluxes in units of counts per second are converted into magnitudes by SOURCEEXTRACTOR using the equation $m = m_{ZP} - 2.5 \times \log(\text{flux})$, where m_{ZP} is the zero-point for each filter (see Table 1). The absolute flux calibration is determined by the calwf3 data-processing pipeline, which produces the calibrated single-visit files (FLCs) that are combined during the drizzle process (Section 3). The HST instruments are exceptionally well characterized, and details of the calwf3 calibrations are described in Section 3 of the Instrument Handbook (Sahu 2021) and Calamida et al. (2022). The flux and magnitude values reported for each filter include the isophotal (ISO) and automatic (AUTO) aperture measurements. The isophotal values use the detection threshold as the lowest isophote, while the automatic measurements are based on the Kron radius (Kron 1980), which encompasses $\geq 90\%$ of the total flux (Infante 1987; Bertin & Arnouts 1996), providing the most precise measurement for extended galaxies (see Figure 4).

The photometric measurements are PSF-matched across all filters, and the background level for each source is determined using a local aperture so that any residual spatial variations

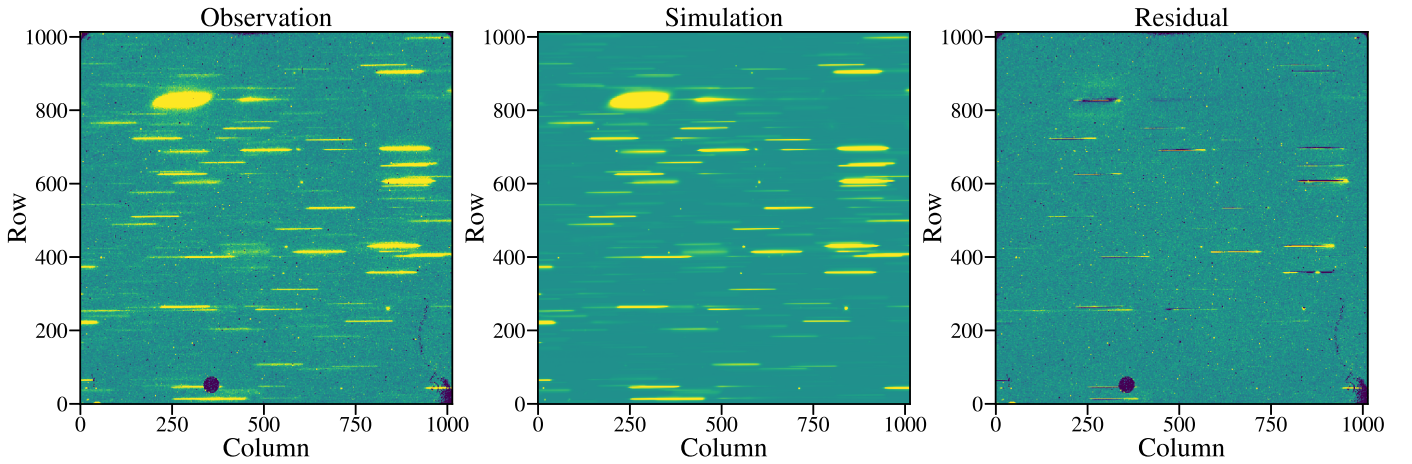


Figure 6. The spectral modeling process for the HST WFC3 G141 grism data, using the example of a single exposure. The three panels show the data (left), simulation (center), and residuals (right). The small residuals for most objects highlight the accuracy of the astrometric alignment, the photometry used in the simulations, and the subtraction of the dispersed background. The circular and curved regions of dead pixels near the bottom of the images are known as the “death star” and “wagon wheel” (see Hilbert & McCullough 2009; Dahlen et al. 2010; Hilbert & Bushouse 2010).

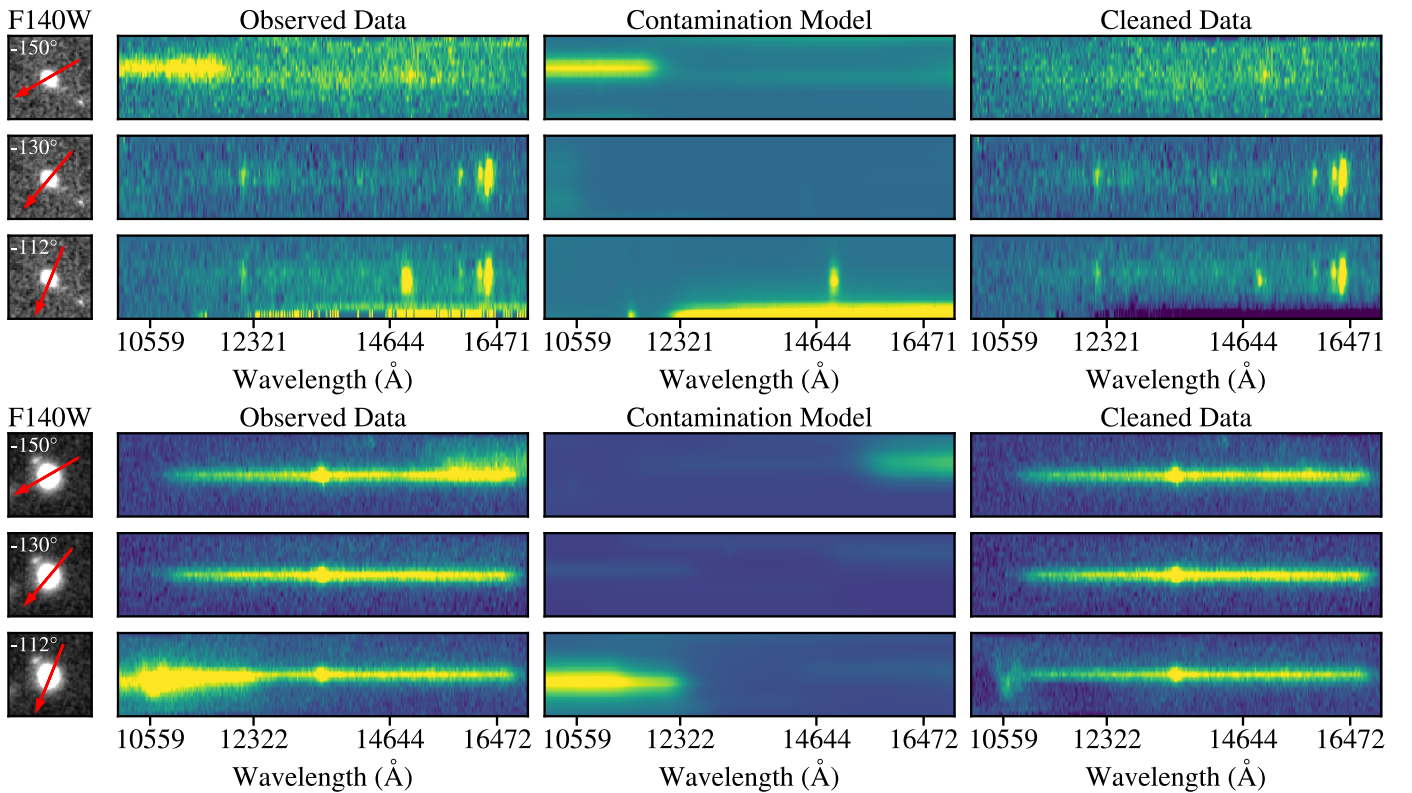


Figure 7. The spectral extraction process for objects 1280 (upper rows) and 1388 (lower rows). The first column shows the F140W image and the dispersion angle for each grism spectrum (red arrows, -150° , -130° , and -112°). The exposures taken at each orientation angle are stacked to produce high S/N 2D spectral images (second column), and the data are binned to $0''.129$ in the spatial direction and 21.5 \AA in the spectral direction to produce a spectrum with linear dispersion. The contamination model that accounts for emission from other sources (third column) is then subtracted from the data, resulting in a cleaned 2D spectral image (fourth column). The 1D spectra are then extracted using an optimal weighting scheme derived from the simulated images (see Pirzkal et al. 2017). The extracted 1D spectra for these objects are shown in Figure 10.

across the mosaics are handled self-consistently. We do not include any correction for Galactic extinction, which is very small for this field, with $E(B - V) \leq 0.018$ (see NASA/IPAC IRSA Resolver²⁹ using the data tag: ADS/IRSA.Dust#2022/1110/082611_30964).

The multiband photometric catalog was then assembled by merging the catalogs for the individual filters and selecting the

columns of primary interest, with a total of 92 columns. The SOURCEEXTRACTOR catalog is available in machine-readable form, and the catalog columns are listed in Table 4.

4.3. Catalog Completeness

We characterized the depths of the images and the completeness of our photometric catalog to empirically determine the fraction of objects that we may expect to detect as a function of apparent magnitude. First, we used the code

²⁹ <https://irsa.ipac.caltech.edu/applications/DataTag/>

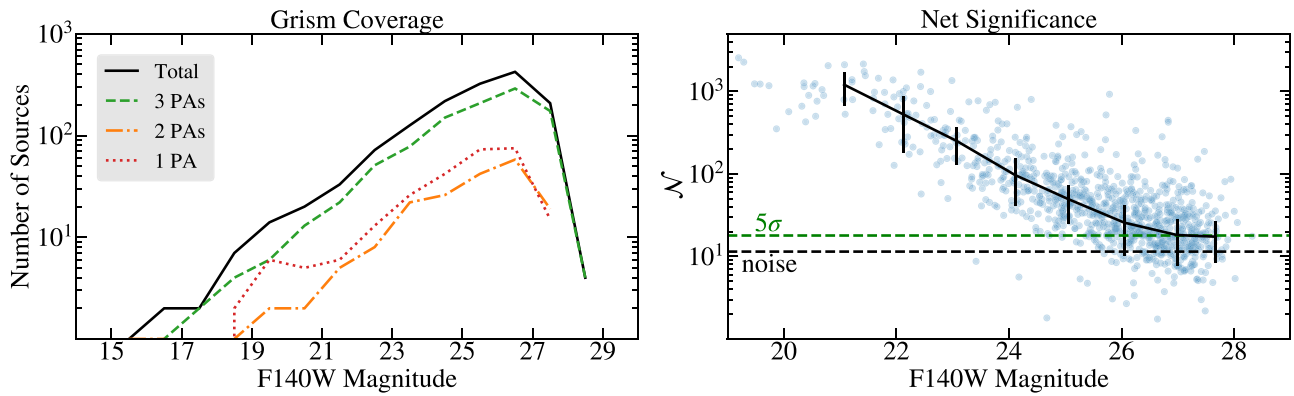


Figure 8. The left graphic shows the number of extracted grism spectra with coverage at one (dotted red), two (dotted–dashed orange), or three (dashed green) position angles as a function of magnitude, with the total shown by the solid black line. The majority of sources ($\sim 70\%$) have coverage in all three pointings. The right graphic shows the net significance (\mathcal{N}), or maximum cumulative S/N for each spectrum as defined in Section 5.2 for sources covered by three PAs. Overall, brighter sources have a higher \mathcal{N} , corresponding to a higher S/N in the continuum and/or emission lines. The dashed black line corresponds to pure noise (no detection), while the dashed green line corresponds to a 5σ detection (see Section 5.2 for details). In general, we detect the continuum emission of sources at $\geq 5\sigma$ confidence ($\mathcal{N} \approx 18$) down to a magnitude limit of $m_{\text{F140W}} \approx 27$.

described in Prichard et al. (2022)³⁰ to determine the image depths. This procedure measures the rms background value in 1000 randomly selected empty sky regions, generates a histogram of the rms values, and then fits the distribution with a Gaussian profile to determine the sigma-clipped median for each image. The median rms value is multiplied by the correlated pixel noise correction factor for that filter, and then converted into a limiting magnitude using the zero-point and a specified aperture size. The correlated pixel noise corrections for each HST filter are listed in Section 3.3, the zero-points are provided in Table 1, and in this case, we used an aperture of $0''.2$ in radius to calculate 5σ limits. The results of this process are listed in Table 1, and we note that the deep portion of the F140W mosaic reaches a 5σ depth of 28.1 ± 0.1 in AB magnitude, which is within ~ 0.2 mag of the exposure time calculator estimate.

We also performed a standard completeness analysis by introducing artificial sources into our images at increasingly fainter magnitudes, and measuring their detection rates with SOURCEEXTRACTOR. We used our PSF models for this purpose, which are already normalized to a total flux of unity, and so by convention have integrated magnitudes equal to the zero-point of their respective filters. We then scale the PSFs to other magnitudes using a simple multiplicative factor. As in Fossati et al. (2019), we then repeated these tests using mock galaxies convolved with the PSF, with Sérsic indices of $n = 2$ inclined at 45° and effective radii of $0''.26$. This size corresponds to ~ 5 kpc at $z \approx 1$, which is typical of star-forming galaxies (Van Rossum & Drake 2009).

The results of this process are shown in Figure 5 and quantified in Table 1, which suggest a slightly shallower limit than the rms procedure. However, this is expected as the PSFs have FWHMs that are smaller than the $0''.4$ diameter apertures used in the rms measurements. The recovered magnitudes quoted in Table 1 are ~ 0.15 mag fainter than the planted values shown in Figure 5, which is consistent with measurements based on the Kron radius (see Section 4.2). The F140W curve is shown for the deep region of the mosaic, and the wide portion follows a similar curve to that of the F125W, which is also one orbit in depth (see Table 1). Despite comparable

exposure times, the F336W is deeper than the F140W due to the lower background levels in the UV. However, galaxies are substantially brighter in the NIR, resulting in a higher S/N for detection.

5. Grism Spectroscopy

5.1. The Simulation-based Extraction Method

We use the simulation-based extraction (SBE) method described in Pirzkal et al. (2017) to extract high-quality spectra that are flux and wavelength calibrated, free from contamination by other sources in any other spectral order, and reach the faintest possible emission line and continuum sensitivities. The SBE method principally relies on our ability to simulate each observation using a combination of photometric measurements and accurate calibration of the dispersion of the grism element. These simulations allow us to properly identify empty regions in each dispersed image so that the underlying background levels can be estimated accurately, and they provide a quantitative estimate of the spectral contamination for each object that is removed during spectral extraction. These models also inherently contain the effect of the line spread function of the grism, which allows us to compute a sensitivity function specific to the morphology of each source. This applies to one-dimensional (1D) spectra that are integrated perpendicular to the dispersion axis, as well as two-dimensional (2D) spectra that contain both wavelength and spatial axes.

In general, the extraction of slitless spectroscopy requires knowing exactly where the spectral trace for every object is dispersed onto the detector, both to extract the flux of the object of interest and to remove contamination of overlapping spectral traces from nearby sources. This requires an accurate measure for the position and size of every object in the field, which is provided by our source catalog in combination with accurate calibrations for the G141 grism dispersing element. The physical size of each object is important because the shape of the dispersed spectrum is a convolution of the object’s radial light profile with the intrinsic spectrum, i.e., emission lines for extended sources will be broader than for an unresolved object. While the grism observations were conducted at three PAs to model and remove contamination from overlapping spectral traces, this means that the 1D spectra at each PA for extended objects will differ in their shape and flux calibration. The SBE

³⁰ https://github.com/lprichard/hst_sky_rms

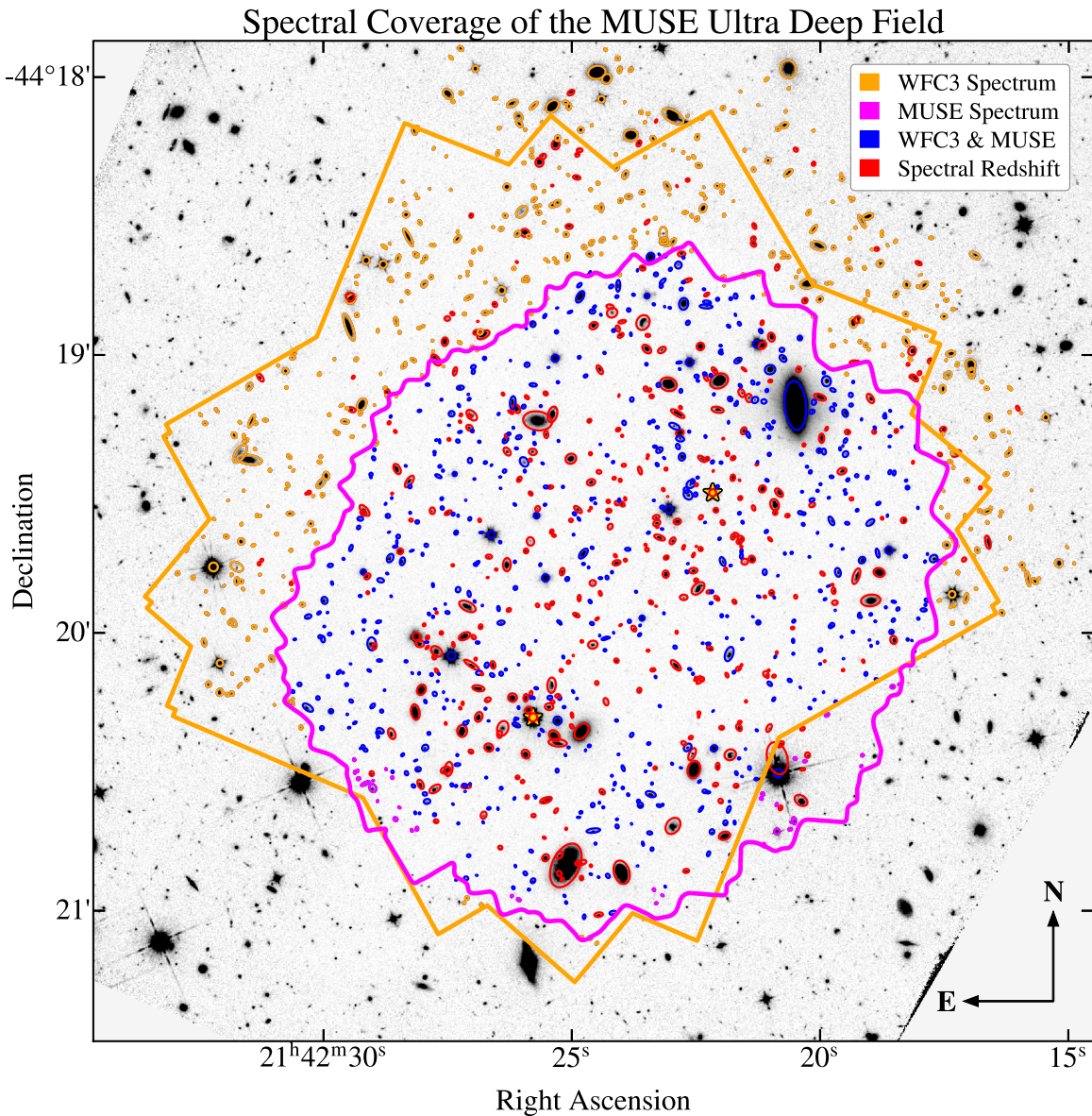


Figure 9. The same FOV as in Figure 2, showing sources with spectroscopic coverage in WFC3 (1499 sources) and MUSE (991 sources). The maximum spatial extent of the WFC3 and MUSE spectral regions is shown by the thick orange and magenta regions, respectively. Objects with spectra are shown with apertures equal to six times their Kron radii, and are colored in the following order: sources in orange have only a WFC3 spectrum (550 sources), magenta sources have only a MUSE spectrum (42 sources), blue sources have both WFC3 and MUSE spectra (949 sources), and red sources have a spectroscopic redshift (419 sources). The WFC3 grism disperses the field such that some sources with spectra are located just outside the direct-imaging FOV, as seen by sources near the top of the figure, and bright objects without redshifts are primarily foreground stars in our Galaxy. These data provide spectroscopic coverage in at least one instrument for 1541 sources, yielding 419 confirmed spectroscopic redshifts.

method accounts for this by using object-specific spectral responses derived from the data, simulations, and photometry, rather than assuming a point-source distribution (see Section 4.2 of Pirzkal et al. 2017). Importantly, the F140W and F125W mosaics are used to derive a spectral slope for each object, which provides an important constraint on the relative fluxes of overlapping spectra during extraction.

We examined the 558 grism exposures and discarded 15 with poor image quality due to jitter during the orbit or satellite trails that could not be masked fully. We used the latest available HST WFC3 G141 grism configuration files (see Pirzkal et al. 2016; WFC3-ISR 2016-15) and the improved background subtraction described in Pirzkal & Ryan (2020; WFC3-ISR 2020-04). The latter allowed us to estimate and

remove the variable He I emission from the Earth’s atmosphere. This He I contamination varies during the course of the observations, as described in Section 2.2, and we carefully removed it before conducting on-the-ramp fitting of the multiple WFC3 reads of each exposure in order to produce a final calibrated image in units of electrons s^{-1} .

We then extracted the grism data using the techniques described above with our segmentation map and source catalog (Section 4), resulting in G141 spectra for 1499 sources. An example of the spectral extraction process is shown in Figures 6 and 7, and the properties of the extracted spectra for the entire sample are summarized in Figure 8. The extracted spectra are sampled at $21.5 \text{ \AA pixel}^{-1}$, which is twice the native dispersion, to take advantage of the many

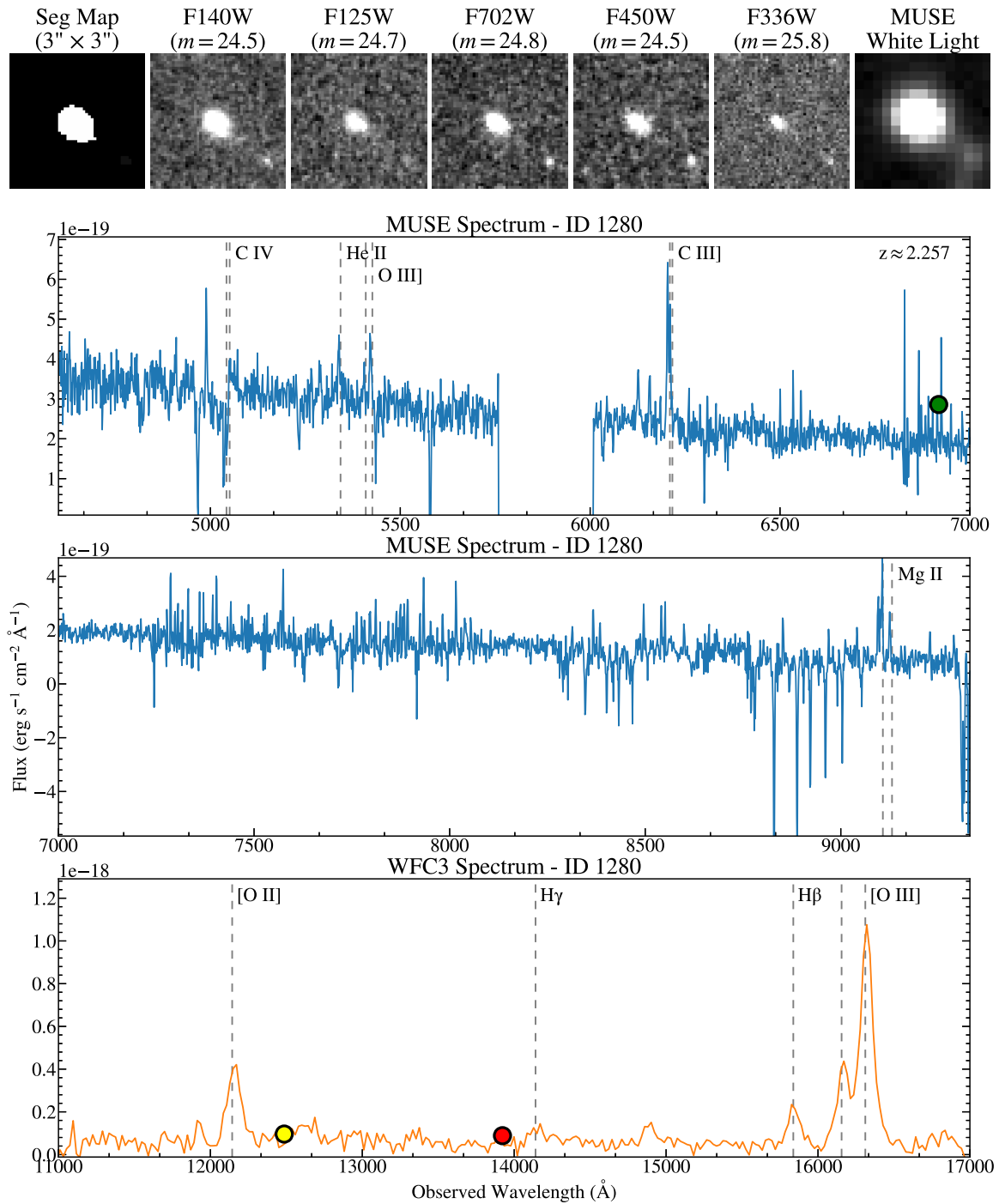


Figure 10. (a) The HST segmentation map, F140W, F125W, F702W, F450W, and F336W imaging, and MUSE white-light image (upper row), MUSE spectroscopy (middle rows in blue), and WFC3 G141 grism spectroscopy (lower row in orange) for object ID 1280, a luminous active galaxy based on emission line ratios, at a redshift of $z \approx 2.257$. The locations of detected emission lines are shown by vertical dashed lines, based on the best-fitting redshift value. The remaining calibration artifacts have negligible effects on the data quality, but include slight deviations in the WFC3 spectrum at the shortest wavelengths due to the decreased sensitivity of the grism, as well as residual skyline absorption features at the longest wavelengths in MUSE. The photometry for each filter is shown (when available) by a filled circle in the order F450W (blue), F702W (green), F125W (yellow), and F140W (red). The fluxes are shown with 3σ uncertainties, which are typically smaller than the size of the points. (b) The same as above for object ID 1388 at a redshift of $z \approx 1.052$.

dither positions. These spectra represent all of the sources contained in the deep central region of the F140W imaging, as well as off-detector sources that are dispersed onto one side of the detector, as shown in Figure 9. Finally, several examples of the extracted grism spectra are shown together with the direct imaging in Figure 10.

5.2. Net Significance

We characterized the quality and sensitivity of our grism spectra by calculating the net significance (\mathcal{N}), or maximum cumulative S/N, for each spectrum. As defined by Pirzkal et al. (2004, 2017), the net significance is calculated by (1) dividing

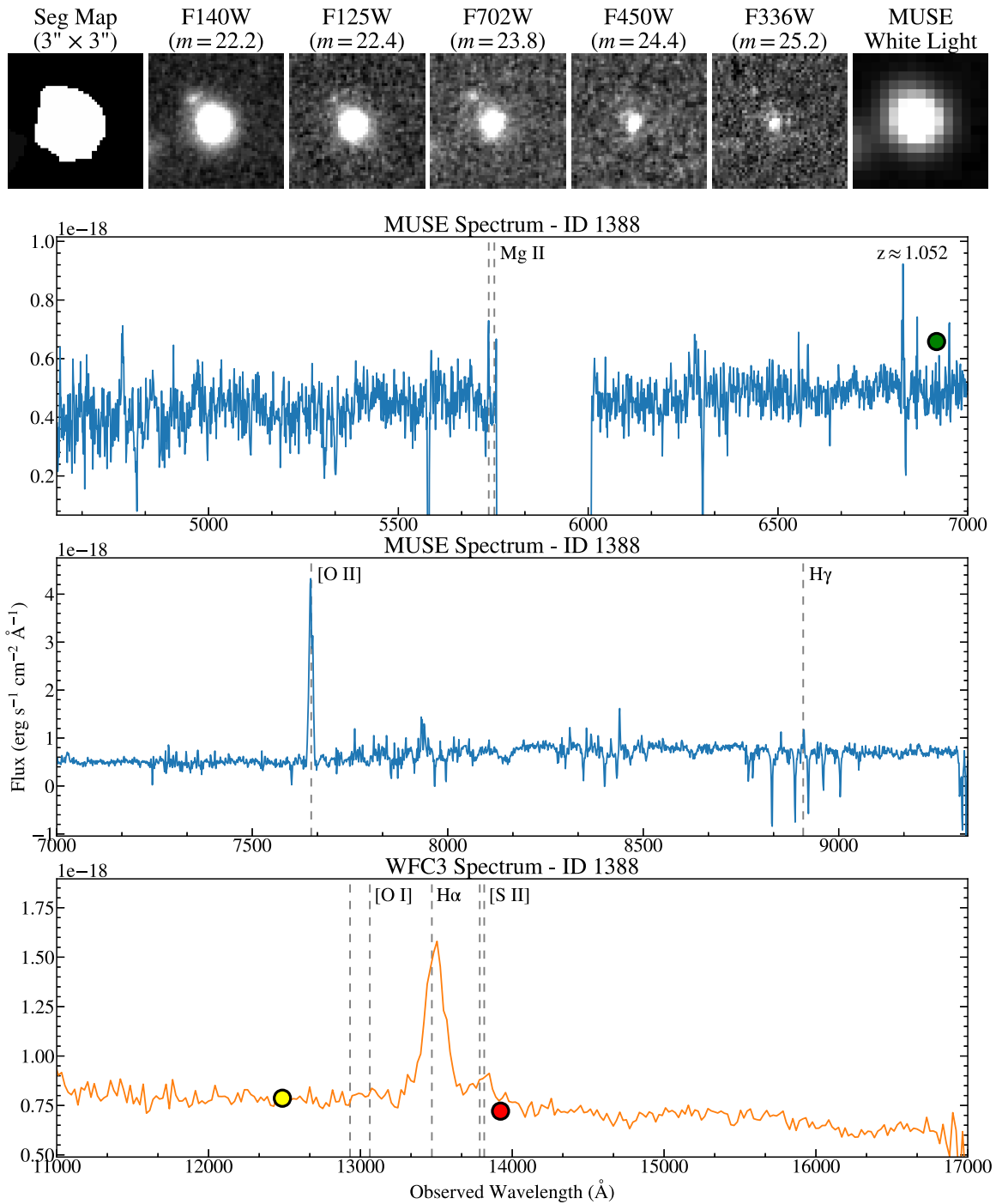


Figure 10. (Continued.)

every flux value by its associated error to produce an array of S/N values, (2) sorting the original flux and error arrays in decreasing order of the S/N estimates, and then (3) computing the cumulative S/N using a successively larger number of bins until the maximum value is reached.

This single value encompasses the information content of a spectrum as compared to pure noise, where a low value implies that there is minimal information above the noise. A high value corresponds to a strong detection of the continuum emission, an isolated emission line feature, or a combination of these two cases. As the pixels are sorted by S/N prior to summation, even a spectrum of pure noise will yield a positive \mathcal{N} value. Based

on Pirzkal et al. (2004), a spectrum of pure Gaussian noise with n_{pix} independent pixels will have $\mathcal{N} = C \times (n_{\text{pix}}/100)^{1/2}$, where $C \approx 6.35 \pm 0.72$ and $n_{\text{pix}} = 325$ for our extracted 1D grism spectra. This implies that a spectrum with $C > 8.5$ in the above relation corresponds to detecting real signal in the data at a 3σ confidence level. However, it is important to emphasize that contamination, detector artifacts, noise properties, and small imperfections in the background subtraction can shift \mathcal{N} to higher or lower values than these theoretical thresholds.

We show the net significance of our spectra as a function of the F140W magnitude in Figure 8. In general, brighter sources have higher values of \mathcal{N} because the continua are well detected, while

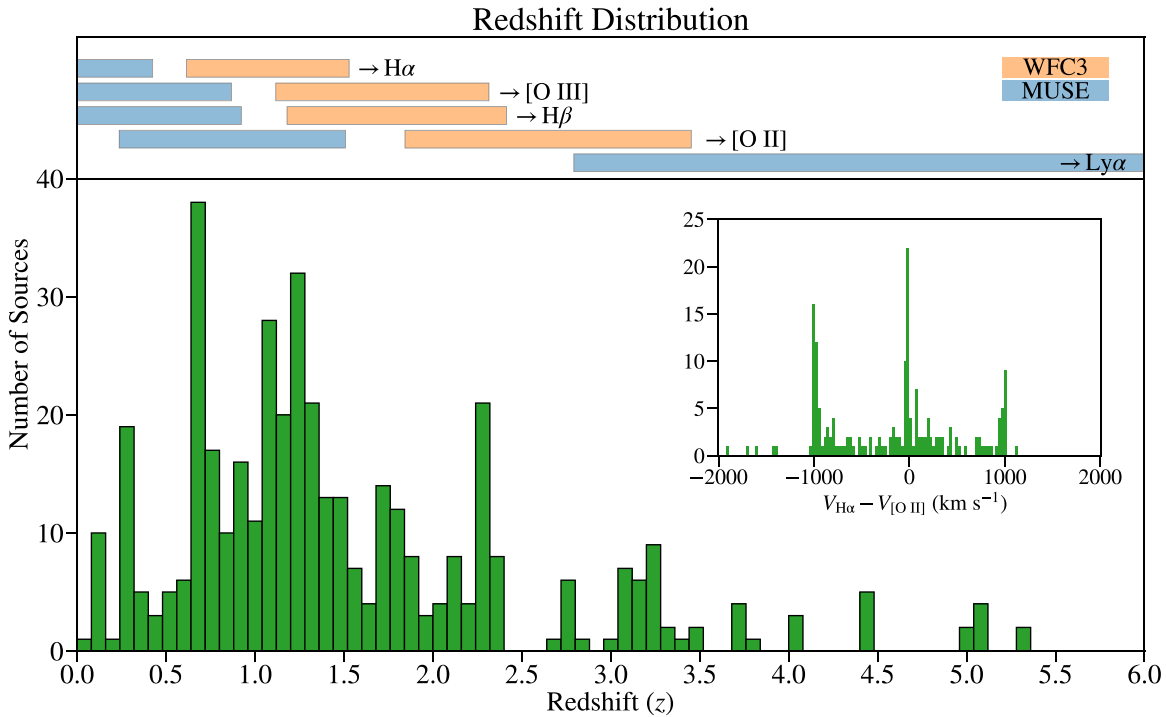


Figure 11. The redshift distribution of sources in the MUDF catalog, with confirmed spectroscopic redshifts for 419 objects. The bins are $\delta z = 0.08$ in width, and sources between $z \approx 0-3$ are of particular interest because they potentially coincide with gas viewed in absorption from the two primary quasars at $z \approx 3.22$. The inset panel shows the differences in redshifts derived from the $H\alpha$ $\lambda 6563$ Å line in WFC3 compared to the $[O\text{ II}]$ $\lambda\lambda 3727, 3729$ Å doublet in MUSE for sources with detections of both emission lines ($0.6 < z < 1.5$). The redshifts of lines in MUSE and WFC3 were constrained to match within ~ 1000 km s^{-1} , except for a few sources for which a larger offset improved the overall fitting result.

fainter sources approach $\mathcal{N} \approx 15$, corresponding to an $\sim 3\sigma$ detection. These characteristics are expected, as the observations were designed so that the depth of the direct imaging matches the faintest sources that can be extracted with confidence. While even deeper imaging would be useful to characterize the contamination of sources detected at the $< 3\sigma$ statistical level, this would have significantly reduced the depth of the grism spectroscopy. The distribution shown in Figure 8 indicates that a 5σ continuum detection limit in the grism data corresponds to a source magnitude of $m_{\text{AB}} \approx 27$ in the F140W mosaic on average.

5.3. Spectroscopic Redshifts

We provide barycentric spectroscopic redshifts for the entire sample in the current source catalog for completeness, and we will describe the spectral fitting process in greater detail in a subsequent publication (M. Revalski et al. 2023, in preparation). In brief, we simultaneously fit the WFC3 and MUSE spectroscopy in order to identify emission line galaxies, determine their spectroscopic redshifts, and measure emission line fluxes. The line fluxes can be used to calculate line ratios that are sensitive to the physical conditions in the gas, including the temperature, density, ionization level, and dust content.

We adopted the interactive spectral fitting routine described in Henry et al. (2021), and modified it to fit a total of 34 emission lines from UV to NIR wavelengths. First, all of the spectra are automatically analyzed with a continuous wavelet transform (CWT), which robustly identifies sources with at least one emission line above a user-defined threshold. This process alleviates the requirement of visually inspecting every spectrum, which is an extremely time-consuming process for large surveys. We found that this process is highly complete, recovering $> 98\%$

Table 5
Redshift Quality Flags

Value	Criteria	Source Count
4	2+ lines with $S/N \geq 5$	366
3	2+ lines with $S/N \geq 3$	22
2	1 line with $S/N \geq 5$	31
1	spectral coverage, but no redshift	1088
99	no spectral coverage for the source	1868

Note. The redshift quality flags used in the source catalog.

of the sources that are identified visually and through other automated line-finding techniques.

Next, a cubic spline is simultaneously fit to the continuum of the WFC3 and MUSE spectra, and the code makes an initial guess of the object redshift based on the strongest emission line. The user can then easily change the guess to other emission lines, adjust the points used in the continuum fit, mask regions of contamination, and then either reject the fit or save the results to an emission line catalog. In the case of objects with only a single emission line, we used the absence of other lines in either WFC3 or MUSE to determine the correct redshift. Specifically, when $H\alpha$ $\lambda 6563$ Å is observed in the grism, then $[O\text{ III}]$ $\lambda 5007$ Å is typically detected in MUSE, while at higher redshifts, $[O\text{ III}]$ is in the grism and the $[O\text{ II}]$ $\lambda 3727$ Å doublet is resolved in MUSE. We will release the emission line catalog in a forthcoming publication, and the resulting redshifts for the sample are shown in Figure 11.

The spectral dispersion of WFC3 and MUSE differ by a factor of ~ 20 , so it is important to consider differences in the redshifts derived from fitting each data set. In the inset of

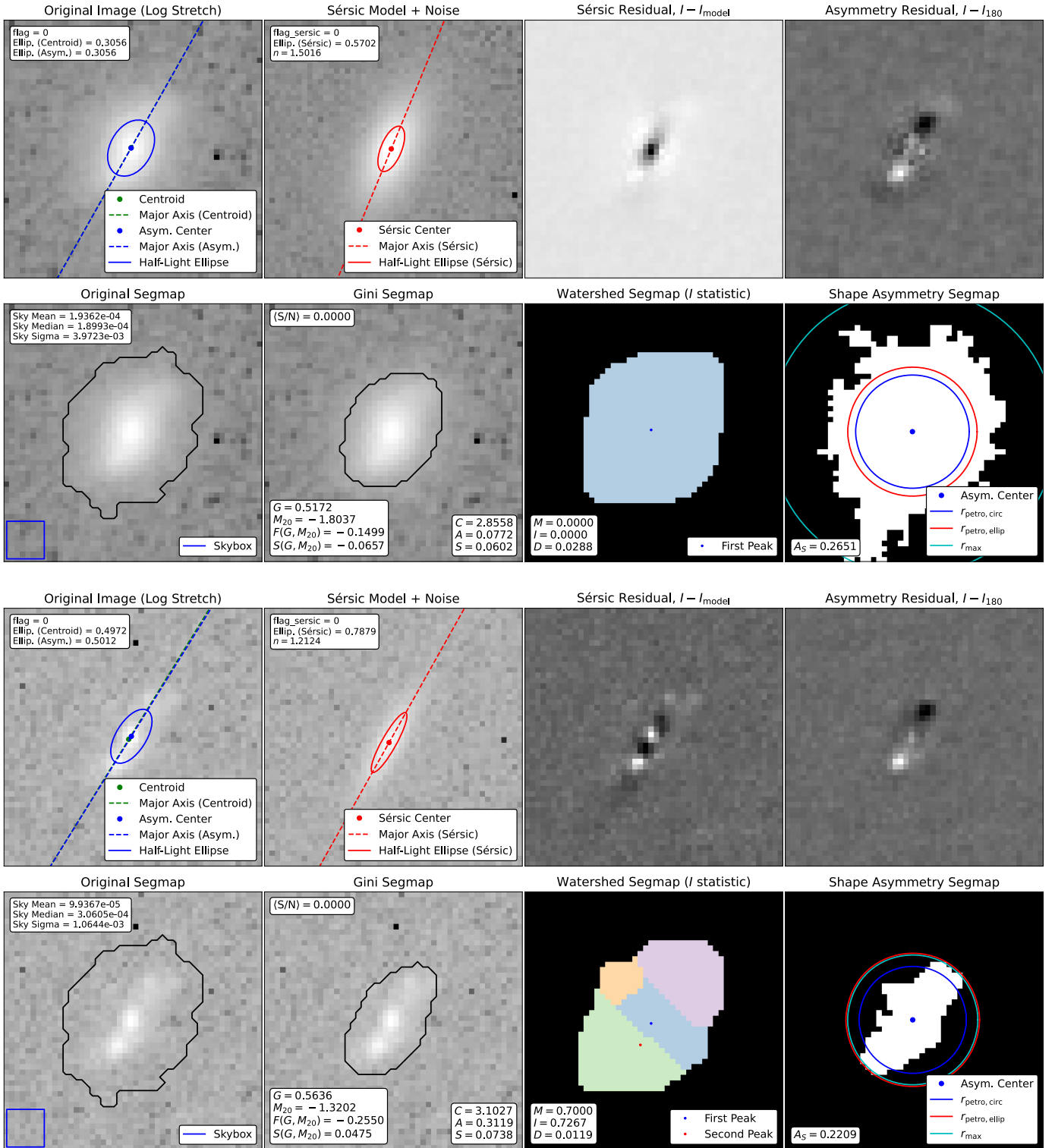


Figure 12. An example of the STATMORPH results for object ID 2499 using the F140W (upper pane) and F336W (lower panel) filters. These figures are produced by the code’s internal MAKE_FIGURES function, and they summarize numerous morphological parameters for each object. The upper left quadrant contains two panels with the best-fit elliptical and Sérsic models, and it displays the orientation and half-light radii for each model. These are subtracted from the image to generate residual maps (upper right quadrant). The lower left quadrant displays the original image with the user-supplied and Gini segmentation maps, while the lower right quadrant provides the watershed segmentation map where each color is associated with a local brightness maximum, followed by the shape asymmetry mask used to calculate the maximum and Petrosian radii. A complete description of the morphological parameters measured by STATMORPH is provided in Section 4 of Rodriguez-Gomez et al. (2019).

Figure 11, we show the difference in velocity between the $H\alpha$ and $[O\text{ II}]$ emission lines for sources where both can be detected. The redshifts were constrained to match within δ

$z \leq 0.00334$ ($\sim 1000 \text{ km s}^{-1}$), except for a few sources. In 83% of the cases, the difference in velocity from $H\alpha$ versus $[O\text{ II}]$ is $< 500 \text{ km s}^{-1}$, in 98% of the cases, they agree within

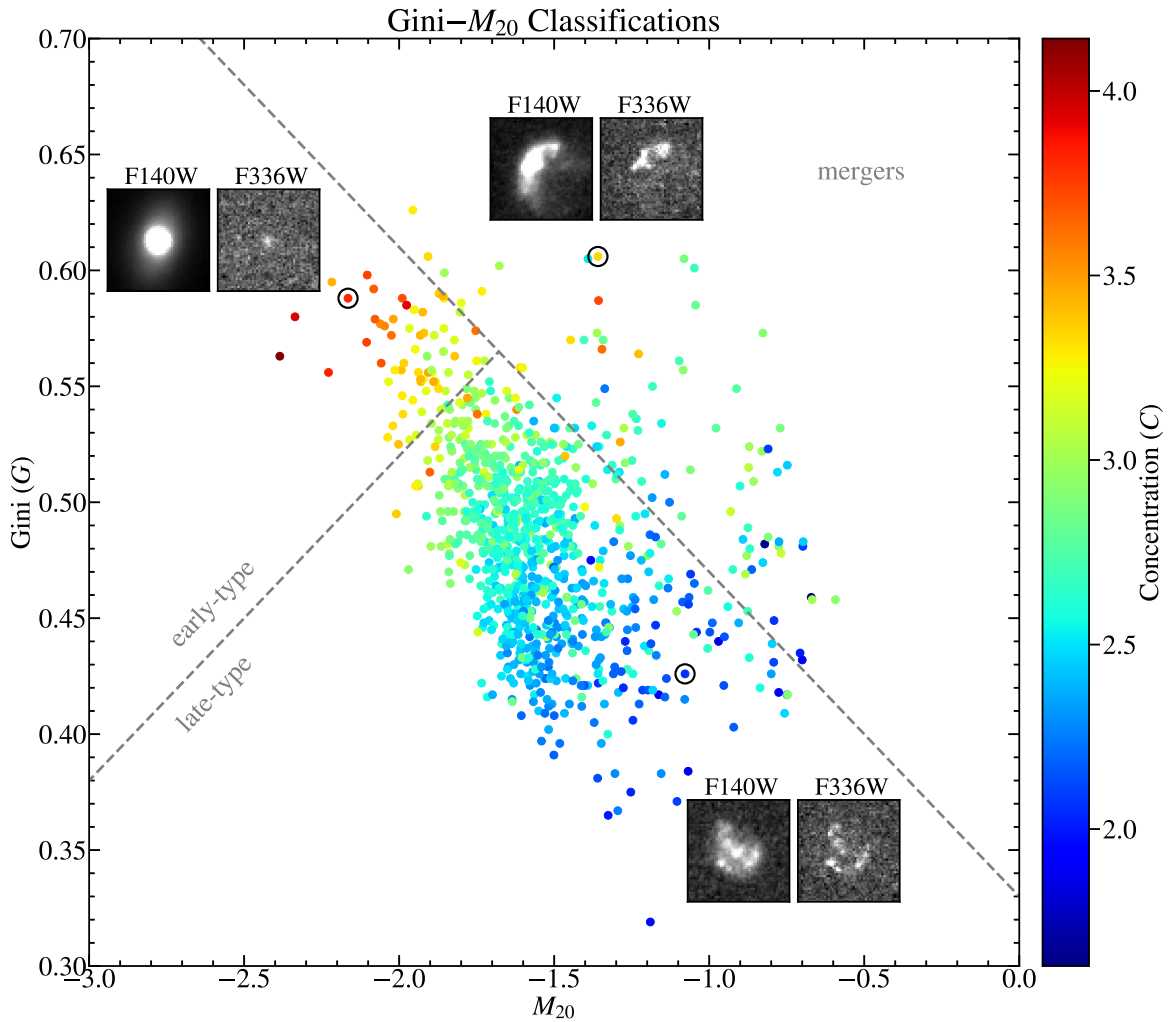


Figure 13. The Gini– M_{20} classification diagram for our sample, color-coded by the concentration index. The dividing lines for early-type, late-type, and merging systems are defined in Lotz et al. (2008) for systems at $z < 1.2$. Galaxies that are classified as early-type in the diagram are usually more concentrated based on their M_{20} values. The inset panels show the F140W and F336W imaging for the sources in black circles.

1000 km s^{-1} , and in 99% of the cases, they agree within 2000 km s^{-1} . The catalog redshifts are based on the resolved [O II] $\lambda\lambda 3727, 3729 \text{ \AA}$ doublet when available, followed by $\text{H}\alpha \lambda 6563 \text{ \AA}$.

Finally, we assign quality flags to the redshift measurements to indicate their confidence levels using the values listed in Table 5. We note that resolved doublets such as [O II] in MUSE and [O III] in WFC3 are treated as two lines because they provide relatively unambiguous redshift measurements.

6. Morphology Measurements

We used the Astropy-affiliated package STATMORPH (v0.4.0; Rodriguez-Gomez et al. 2019) to derive nonparametric morphological measurements for the sources in our photometric catalog. While SOURCEEXTRACTOR measures some similar parameters, STATMORPH can also use a PSF model to measure more accurate sizes for compact sources, and provides additional diagnostics, such as the Sérsic index (Sersic 1968), as well as concentration, asymmetry, and smoothness (CAS) statistics (Bershady et al. 2000; Conselice 2003; Lotz et al. 2004). The nonparametric formalism of STATMORPH has the advantage that many morphological parameters are reported

without assuming a particular functional form for the underlying distributions of these parameters.

An example of the morphological analysis for one object is shown in Figure 12, with the significance of each parameter described in Rodriguez-Gomez et al. (2019), and here we provide a brief overview. The code calculates a variety of size and shape measurements relative to the flux, asymmetry, and Sérsic centroids of each object. The reported sizes include measures such as half-light radii (r_{half} , r_{50}), the Petrosian radius (r_{petro} , Petrosian 1976), and the second moment of each galaxy’s brightest regions containing 20% of the flux (M_{20}). STATMORPH also provides concentration (C), asymmetry (A), and smoothness (S) statistics, along with the Gini index (G), which provides unique metrics for characterizing nonuniform distributions of light (Conselice 2014; Pawlik 2014).

We used the code with our segmentation map, full five-filter mosaics, and PSF models, in order to quantify how the morphologies of the sources change as a function of the observed wavelength. The F140W and F336W filters are particularly useful because they provide spatially matched measurements of the rest-frame optical and UV emission for ~ 1580 sources across a range of redshifts. As described in Rodriguez-Gomez et al. (2019), the code has several flags that

Table 6
Morphology Catalog Columns

Column Number	STATMORPH Parameter
(1)	id
(2)	flag
(3)	flag_sersic
(4)	flag_catastrophic
(5)	xc_centroid
(6)	yc_centroid
(7)	elongation_centroid
(8)	orientation_centroid
(9)	ellipticity_centroid
(10)	concentration
(11)	asymmetry
(12)	smoothness
(13)	rhalf_circ
(14)	rpetro_circ
(15)	sersic_n
(16)	sersic_theta
(17)	sersic_ellip
(18)	sersic_amplitude
(19)	sersic_rhalf
(20)	gini
(21)	m20

Note. The STATMORPH parameters included in our catalog, with the exact definitions provided in Section 4 of Rodriguez-Gomez et al. (2019).

report the quality of the fitted results for each object, with zero indicating success, and unity indicating a possible issue.

We provide the STATMORPH results in the form of machine-readable tables and code-generated figures that highlight key properties of the fit, including the object segmentation, major axis, Sérsic index (when available), and CAS statistics. We only report the results for objects with a successful fit ($\text{flag} = 0$), with most of these also having a derived Sérsic index ($\text{flag_sersic} = 0$). Cases in which the basic fit was successful, but a Sérsic index could not be robustly derived as determined by the code are indicated in the table with $\text{flag_sersic} = 1$.

The parameters reported by STATMORPH can be used in combination to distinguish objects of different morphological types. One example is the widely used Gini- M_{20} classification system (Lotz et al. 2004, 2008), which approximately separates early-type (E, S0, and Sa), late-type (Sb, Sc, Sd, and Irr), and merging galaxies, although how the Gini- M_{20} plane is divided into these three regions varies across the literature (e.g., Snyder et al. 2015; Rodriguez-Gomez et al. 2019). We constructed this diagnostic diagram for our sample and show the results in Figure 13. As expected, galaxies that are classified as early type based on their position in the Gini- M_{20} diagram tend to contain most of their light in the central regions, lending confidence to the STATMORPH-derived properties. These measurements provide crucial morphological information for understanding the properties of galaxies in different environments, particularly as a function of observed wavelength, which will be further investigated in future work.

7. High Level Science Products

In Table 7 we document the files that are publicly available as HLSPs from the MAST portal. The data products encompass three categories: imaging, spectroscopy, and catalogs. The

imaging includes our science drizzles, PSF models, convolution kernels, PSF-matched drizzles, and the segmentation map. The spectroscopy includes the calibrated 1D spectra and the 2D spectral images. Our catalogs include the multifilter photometric catalog created with SOURCEEXTRACTOR and the STATMORPH morphological catalog. Detailed descriptions of the data reduction and analysis techniques used to produce these data products are contained in Sections 3–6, and their key characteristics are provided in Tables 1–6. We reiterate that users may wish to apply their preferred correction for Galactic extinction to the photometry, although it is very small for this field (see Section 4.2). In Table 7 we provide a list of the filename extensions for each type of data product, with files provided in the Flexible Image Transport System (FITS) format. The catalogs are provided in simple tabular text file formats. These HLSPs can be accessed from the MAST portal using the DOI [10.17909/81fp-2g44](https://doi.org/10.17909/81fp-2g44). The files are also described on the MAST project web page at <https://archive.stsci.edu/hlsp/mudf>.

8. Summary

The MUSE Ultra Deep Field hosts two associated quasars at $z \approx 3.22$ that provide a unique laboratory for connecting the physical properties of galaxies seen in emission with their surrounding gas observed in absorption. We have observed this field over 90 orbits in a single pointing with the HST WFC3/IR G141 grism and F140W filter, comprising the deepest HST grism survey ever conducted for a single field. We combined WFC3 (F140W, F125W, and F336W) and archival WFPC2 (F702W and F450W) imaging to detect 3375 sources, with 1536 having both spectroscopic and photometric coverage. The F140W and F336W mosaics reach depths of $m_{\text{AB}} \approx 28$ and 29, respectively, providing NIR and rest-frame ultraviolet data for 1580 sources, and we reach 5σ continuum detections in the grism spectra for objects as faint as $m_{\text{AB}} \approx 27$. By using the long-wavelength coverage of the MUSE and WFC3 spectroscopy, we derived robust spectroscopic redshifts for 419 galaxies between $z \approx 0$ –6.

We have generated custom-calibrated science images, photometric and morphological catalogs, and high-legacy value data products for the MUSE Ultra Deep Field that are available to the community through the MAST portal. These data products enable numerous studies aimed at advancing our models of galaxy formation and evolution in different environments. Specifically, we aim to connect the physical properties of the IGM and CGM traced in absorption with the galaxies discovered in emission to obtain a full census of the gas in and around galaxies in field, group, and candidate protocluster environments. Our forthcoming investigations include connecting the metal enrichment of the IGM and CGM with the gas phase metallicities of low-mass galaxies over cosmic time.

The authors would like to thank the anonymous reviewer for helpful comments that improved the clarity of this paper.

M.R. thanks Jay Anderson and Varun Bajaj for discussions on PSF modeling, Mihai Cara for assistance in drizzling WFPC2 data, Xin Wang for helpful discussions on PSF convolution window functions, Roberto J. Avila for Astropy WCS assistance, Edward Slavich for help in code parallelization, and Vicente Rodriguez-Gomez for STATMORPH support.

Table 7
MAST HLSP Filename Extensions

Extension	Description
* DRZ_SCI	The science drizzles with pixel scales of 0''.06 per pixel and units of counts per second.
* DRZ_WHT	The drizzle weight maps produced using the inverse variance map (IVM) option in AstroDrizzle.
* DRZ_RMS	The drizzle error maps that are defined as $1/\sqrt{IVM}$ and have been corrected for correlated pixel noise.
* DRZ_NEG	The science drizzles multiplied by -1.0 so they may be used to determine source detection thresholds.
* PSF_MOD	The area normalized PSF models that are 69×69 pixels in size with scales of 0''.06 per pixel.
* CON_KER	The area normalized convolution kernels used to PSF-match each filter to the F140W mosaic resolution.
* DRZ_CON	The science drizzles convolved to the spatial resolution of the F140W mosaic and used for photometry.
* SEG_MAP	The merged deep + shallow segmentation map with IDs matching those in the merged source catalog.
* 1D_SPEC	The position angle combined HST WFC3/IR G141 1D spectrum for each object.
* 2D_SPEC	The position angle combined HST WFC3/IR G141 2D spectrum for each object.
* SOURCE_CATALOG	The multifilter SOURCEEXTRACTOR object catalog with the columns listed in Table 4.
* MORPHOLOGY_CATALOG	The STATMORPH morphology catalog for each filter with the columns listed in Table 6.

Note. The files in the HLSP distribution consist of science images (*_FITS), the primary multifilter source catalog (HLSP_MUFD_SOURCE_CATALOG), and morphology catalogs for each filter (*MORPHOLOGY_CATALOG). The science image filenames begin with HLSP_MUFD_HST_WFC3_*, followed by the filter name, version number, and extensions listed above. The 1D spectral files contain multiple extensions (ext.) and we adopt WAVELENGTH, WAVG_OPT, and WSTD_OPT for our wavelengths, fluxes, and uncertainties, where W*_OPT refers to the weighted, optimally extracted values. The 2D spectral files contain the data, uncertainties, contamination model, and cleaned data in ext. 2–5, respectively, with WAVELENGTH in ext. 9.

Based on observations with the NASA/ESA Hubble Space Telescope obtained from the MAST Data Archive at the Space Telescope Science Institute, which is operated by the Association of Universities for Research in Astronomy, Incorporated, under NASA contract NAS5-26555. Support for program Nos. 15637 and 15968 was provided through a grant from the STScI under NASA contract NAS5-26555. These observations are associated with program Nos. 6631, 15637, and 15968.

The MUSE portion of this project has received funding from the European Research Council (ERC) under the European Union’s Horizon 2020 research and innovation program (grant agreement No. 757535) and by Fondazione Cariplo (grant No. 2018-2329).

P.D. acknowledges support from the NWO grant 016.VIDI.189.162 (“ODIN”) and the European Commission’s and University of Groningen’s CO-FUND Rosalind Franklin program and warmly thanks the Institute for Advanced Study (IAS) Princeton, where a part of this work was carried out, for their generous hospitality and support through the Bershadsky Fund.

This research has made use of NASA’s Astrophysics Data System. This research has made use of the NASA/IPAC Infrared Science Archive, which is funded by the National Aeronautics and Space Administration and operated by the California Institute of Technology. This research made use of ccdproc, an Astropy package for image reduction (Craig et al. 2021).

Facilities: HST (WFC3, WFPC2), VLT (MUSE), IRSA.

Software: create_neg_rms_images (Revalski 2022a), hst_wfc3_lacosmic (Revalski 2022b), hst_wfc3_psf_modeling (Revalski 2022c), Astropy (Astropy Collaboration et al. 2013, 2018), DrizzlePac (Hoffmann et al. 2021), IDL (<https://www.harrisgeospatial.com/Software-Technology/>), Jupyter (Kluyver et al. 2016), Matplotlib (Hunter 2007; Caswell et al. 2021), NumPy (Harris et al. 2020), Python (Van Rossum & Drake 2009, <https://www.python.org/>), Scipy (Virtanen et al. 2020a, 2020b), SExtractor (Bertin & Arnouts 1996), Statmorph (Rodriguez-Gomez et al. 2019; <https://statmorph.readthedocs.io/en/latest/>).

Github repositories cited in this publication:

1. https://github.com/mrevalski/create_neg_rms_images (see Revalski 2022a)
2. https://github.com/mrevalski/hst_wfc3_lacosmic (see Revalski 2022b)
3. https://github.com/mrevalski/hst_wfc3_psf_modeling (see Revalski 2022c)
4. <https://github.com/bsunnquist/uvis-skydarks>
5. https://github.com/lprichard/HST_FLC_corrections
6. https://github.com/lprichard/hst_sky_rms

ORCID iDs

Mitchell Revalski  <https://orcid.org/0000-0002-4917-7873>
 Marc Rafelski  <https://orcid.org/0000-0002-9946-4731>
 Michele Fumagalli  <https://orcid.org/0000-0001-6676-3842>
 Matteo Fossati  <https://orcid.org/0000-0002-9043-8764>
 Norbert Pirzkal  <https://orcid.org/0000-0003-3382-5941>
 Ben Sunnquist  <https://orcid.org/0000-0003-3759-8707>
 Laura J. Prichard  <https://orcid.org/0000-0002-0604-654X>
 Alaina Henry  <https://orcid.org/0000-0002-6586-4446>
 Micaela Bagley  <https://orcid.org/0000-0002-9921-9218>
 Rajeshwari Dutta  <https://orcid.org/0000-0002-6095-7627>
 Giulia Papini  <https://orcid.org/0000-0002-5810-318X>
 Fabrizio Arrigoni Battaia  <https://orcid.org/0000-0002-4770-6137>
 Valentina D’Odorico  <https://orcid.org/0000-0003-3693-3091>
 Pratika Dayal  <https://orcid.org/0000-0001-8460-1564>
 Vicente Estrada-Carpenter  <https://orcid.org/0000-0001-8489-2349>
 Emma K. Lofthouse  <https://orcid.org/0000-0002-1209-9680>
 Elisabetta Lusso  <https://orcid.org/0000-0003-0083-1157>
 Simon L. Morris  <https://orcid.org/0000-0003-4866-110X>
 Kalina V. Nedkova  <https://orcid.org/0000-0001-5294-8002>
 Casey Papovich  <https://orcid.org/0000-0001-7503-8482>
 Celine Peroux  <https://orcid.org/0000-0002-4288-599X>

References

- Arsenault, R., Madec, P. Y., Hubin, N., et al. 2008, *Proc. SPIE*, 7015, 701524
- Astropy Collaboration, Robitaille, T. P., Tollerud, E. J., et al. 2013, *A&A*, 558, A33
- Astropy Collaboration, Price-Whelan, A. M., Sipőcz, B. M., et al. 2018, *AJ*, 156, 123
- Atek, H., Furtak, L. J., Oesch, P., et al. 2022, *MNRAS*, 511, 4464
- Atek, H., Malkan, M., McCarthy, P., et al. 2010, *ApJ*, 723, 104
- Atek, H., Siana, B., Scarlata, C., et al. 2011, *ApJ*, 743, 121
- Backhaus, B. E., Bridge, J. S., Trump, J. R., et al. 2023, *ApJ*, 943, 37
- Bacon, R., Accardo, M., Adjali, L., et al. 2010, *Proc. SPIE*, 7735, 773508
- Bacon, R., Mary, D., Garel, T., et al. 2021, *A&A*, 647, A107
- Bacon, R., Brinchmann, J., Conseil, S., et al. 2023, *A&A*, 670, A4
- Bechtold, J. 2001, arXiv:astro-ph/0112521
- Beckett, A., Morris, S. L., Fumagalli, M., et al. 2021, *MNRAS*, 506, 2574
- Bershady, M. A., Jangren, A., & Conselice, C. J. 2000, *AJ*, 119, 2645
- Bertin, E., & Arnouts, S. 1996, *A&AS*, 117, 393
- Bielby, R. M., Stott, J. P., Cullen, F., et al. 2019, *MNRAS*, 486, 21
- Bouwens, R. J., Smit, R., Labbe, I., et al. 2016, *ApJ*, 831, 176
- Bowman, W. P., Ciardullo, R., Zeimann, G. R., et al. 2021, *ApJ*, 920, 78
- Brammer, G. 2019, Grizli: Grism redshift and line analysis software, Astrophysics Source Code Library, ascl:1905.001
- Brammer, G. B., van Dokkum, P. G., Franx, M., et al. 2012, *ApJS*, 200, 13
- Calamida, A., Bajaj, V., Mack, J., et al. 2022, *AJ*, 164, 32
- Casali, M., Pirard, J.-F., Kissler-Patig, M., et al. 2006, *Proc. SPIE*, 6269, 62690W
- Caswell, T. A., Droettboom, M., Lee, A., et al. 2021, matplotlib/matplotlib: REL: v3.5.0, Zenodo, doi:10.5281/zenodo.5706396
- Chadayammuri, U., Bogdan, A., Oppenheimer, B. D., et al. 2022, *ApJL*, 936, L15
- Chen, H.-W., Helsby, J. E., Gauthier, J.-R., et al. 2010, *ApJ*, 714, 1521
- Chen, H.-W., Zahedy, F. S., Boettcher, E., et al. 2020, *MNRAS*, 497, 498
- Colbert, J. W., Teplitz, H., Atek, H., et al. 2013, *ApJ*, 779, 34
- Conselice, C. J. 2003, *ApJS*, 147, 1
- Conselice, C. J. 2014, *ARA&A*, 52, 291
- Cooper, T. J., Rudie, G. C., Chen, H.-W., et al. 2021, *MNRAS*, 508, 4359
- Corlies, L., Peeples, M. S., Tumlinson, J., et al. 2020, *ApJ*, 896, 125
- Craig, M., Crawford, S., Seifert, M., et al. 2021, astropy/ccdproc: v2.1.0 (re-release for Zenodo), Zenodo, doi:10.5281/zenodo.4588034
- Crighton, N. H. M., Bielby, R., Shanks, T., et al. 2011, *MNRAS*, 414, 28
- Dahlen, T., Dressel, L., & Kalirai, J. 2010, Dithering Strategies for WFC3, Instrument Science Report, WFC3 2010-09
- Dayal, P., & Ferrara, A. 2018, *PhR*, 780, 1
- Dekker, H., D'Odorico, S., Kaufer, A., Delabre, B., & Kotzlowski, H. 2000, *Proc. SPIE*, 4008, 534
- D'Odorico, V., Petitjean, P., & Cristiani, S. 2002, *A&A*, 390, 13
- Dutta, R., Fumagalli, M., Fossati, M., et al. 2020, *MNRAS*, 499, 5022
- Dutta, R., Fumagalli, M., Fossati, M., et al. 2021, *MNRAS*, 508, 4573
- Estrada-Carpenter, V., Papovich, C., Momcheva, I., et al. 2019, *ApJ*, 870, 133
- Fielding, D., Quataert, E., McCourt, M., & Thompson, T. A. 2017, *MNRAS*, 466, 3810
- Fossati, M., Fumagalli, M., Lofthouse, E. K., et al. 2019, *MNRAS*, 490, 1451
- Fossati, M., Fumagalli, M., Lofthouse, E. K., et al. 2021, *MNRAS*, 503, 3044
- Francis, P., Dopita, M. A., Colbert, J. W., et al. 2013, *MNRAS*, 428, 28
- Francis, P. J., & Hewett, P. C. 1993, *AJ*, 105, 1633
- Francis, P. J., Williger, G. M., Collins, N. R., et al. 2001, *ApJ*, 554, 1001
- Fruchter, A. S., & Hook, R. N. 2002, *PASP*, 114, 144
- Brown, A. G. A., Vallenari, A., Prusti, T., et al. 2021, *A&A*, 649, A1
- Gonzaga, S., Hack, W., Fruchter, A., & Mack, J. 2012, *The DrizzlePac Handbook* (Baltimore, MD: Space Telescope Science Institute)
- Guo, Y., Ferguson, H. C., Giavalisco, M., et al. 2013, *ApJS*, 207, 24
- Harris, C. R., Millman, K. J., van der Walt, S. J., et al. 2020, *Natur*, 585, 357
- Henry, A., Rafelski, M., Sunquist, B., et al. 2021, *ApJ*, 919, 143
- Hilbert, B., & Bushouse, H. 2010, WFC3/IR Bad Pixel Table: Update Using Cycle 17 Data, Instrument Science Report, WFC3 2010-13
- Hilbert, B., & McCullough, P. R. 2009, WFC3 SMOV Program 11420: IR Channel Functional Tests, Instrument Science Report, WFC3 2009-23
- Hoffmann, S. L., Mack, J., Avila, R., et al. 2021, AAS Meeting, 53, 216.02
- Holtzman, J. A., Burrows, C. J., Casertano, S., et al. 1995a, *PASP*, 107, 1065
- Holtzman, J. A., Hester, J. J., Casertano, S., et al. 1995b, *PASP*, 107, 156
- Hunter, J. D. 2007, *CSE*, 9, 90
- Infante, L. 1987, *A&A*, 183, 177
- Jansen, F., Lumb, D., Altieri, B., et al. 2001, *A&A*, 365, L1
- Khare, P. 2013, *BASI*, 41, 41
- Kimble, R. A., MacKenty, J. W., O'Connell, R. W., & Townsend, J. A. 2008, *Proc. SPIE*, 7010, 70101E
- Kissler-Patig, M., Pirard, J.-F., Casali, M., et al. 2008, *A&A*, 491, 941
- Kluyver, T., Ragan-Kelley, B., Pérez, F., et al. 2016, in *Positioning and Power in Academic Publishing: Players, Agents and Agendas*, ed. F. Loizides & B. Schmidt (Amsterdam: IOS Press), 87
- Kron, R. G. 1980, *ApJS*, 43, 305
- Lochhaas, C., Tumlinson, J., O'Shea, B. W., et al. 2021, *ApJ*, 922, 121
- Lofthouse, E. K., Fumagalli, M., Fossati, M., et al. 2020, *MNRAS*, 491, 2057
- Lofthouse, E. K., Fumagalli, M., Fossati, M., et al. 2023, *MNRAS*, 518, 305
- Lotz, J. M., Primack, J., & Madau, P. 2004, *AJ*, 128, 163
- Lotz, J. M., Davis, M., Faber, S. M., et al. 2008, *ApJ*, 672, 177
- Lusso, E., Fumagalli, M., Fossati, M., et al. 2019, *MNRAS*, 485, L62
- MacAlpine, G. M., Smith, S. B., & Lewis, D. W. 1977, *ApJS*, 34, 95
- MacKenty, J. W., Kimble, R. A., O'Connell, R. W., & Townsend, J. A. 2010, *Proc. SPIE*, 7731, 77310Z
- Maiolino, R., & Mannucci, F. 2019, *A&ARv*, 27, 3
- McCully, C., & Tewes, M. 2019, Astro-SCRAPPY: Speedy Cosmic Ray Annihilation Package in Python, Astrophysics Source Code Library, ascl:1907.032
- McCully, C., Crawford, S., Kovacs, G., et al. 2018, Astropy/Astroscrappy: v1.0.5, Zenodo, doi:10.5281/zenodo.1482019
- Momcheva, I. G., Brammer, G. B., van Dokkum, P. G., et al. 2016, *ApJS*, 225, 27
- Naab, T., & Ostriker, J. P. 2017, *ARA&A*, 55, 59
- Noiroi, G., Sawicki, M., Abraham, R., et al. 2022, *MNRAS*, 512, 3566
- Oke, J. B., & Gunn, J. E. 1983, *ApJ*, 266, 713
- Olszewski, H., & Mack, J. 2021, WFC3/IR Blob Flats, Instrument Science Report, WFC3 2021-10
- Oppenheimer, B. D., Bogdán, A., Crain, R. A., et al. 2020, *ApJL*, 893, L24
- Pandya, V., Fielding, D. B., Bryan, G. L., et al. 2022, arXiv:2211.09755
- Papovich, C., Simons, R. C., Estrada-Carpenter, V., et al. 2022, *ApJ*, 937, 22
- Paufique, J., Bruton, A., Glindemann, A., et al. 2010, *Proc. SPIE*, 7736, 77361P
- Pawlik, M. 2014, *A&G*, 55, 6.13
- Peeples, M. S., Corlies, L., Tumlinson, J., et al. 2019, *ApJ*, 873, 129
- Peroux, C., & Howk, J. C. 2020, *ARA&A*, 58, 363
- Péroux, C., Weng, S., Karki, A., et al. 2022, *MNRAS*, 516, 5618
- Petrosian, V. 1976, *ApJL*, 210, L53
- Pharo, J., Malhotra, S., Rhoads, J., et al. 2019, *ApJ*, 874, 125
- Pharo, J., Malhotra, S., Rhoads, J. E., et al. 2020, *ApJ*, 888, 79
- Pirard, J.-F., Kissler-Patig, M., Moorwood, A., et al. 2004, *Proc. SPIE*, 5492, 1763
- Pirzkal, N., & Ryan, R. 2020, The Dispersed Infrared Background in WFC3 G102 and G141 Observations, Instrument Science Report, WFC3 2020-4
- Pirzkal, N., Ryan, R., & Brammer, G. 2016, Trace and Wavelength Calibrations of the WFC3 G102 and G141 IR Grisms, Instrument Science Report, WFC3 2016-15
- Pirzkal, N., Xu, C., Malhotra, S., et al. 2004, *ApJS*, 154, 501
- Pirzkal, N., Rothberg, B., Ly, C., et al. 2013, *ApJ*, 772, 48
- Pirzkal, N., Malhotra, S., Ryan, R. E., et al. 2017, *ApJ*, 846, 84
- Planck Collaboration, Aghanim, N., Akrami, Y., et al. 2020, *A&A*, 641, A6
- Prichard, L. J., Rafelski, M., Cooke, J., et al. 2022, *ApJ*, 924, 14
- Prusti, T., de Bruijne, J. H. J., Brown, A. G. A., et al. 2016, *A&A*, 595, A1
- Rafelski, M., Teplitz, H. I., Gardner, J. P., et al. 2015, *AJ*, 150, 31
- Rahmati, A., Schaye, J., Crain, R. A., et al. 2016, *MNRAS*, 459, 310
- Revalski, M. 2022a, mrevalski/create_neg_rms_images: v1.0.0, Zenodo, doi:10.5281/zenodo.7458442
- Revalski, M. 2022b, mrevalski/hst_wfc3_lacosmic: v1.0.0, Zenodo, doi:10.5281/zenodo.7458507
- Revalski, M. 2022c, mrevalski/hst_wfc3_psf_modeling: v1.0.0, Zenodo, doi:10.5281/zenodo.7458566
- Rodriguez-Gomez, V., Snyder, G. F., Lotz, J. M., et al. 2019, *MNRAS*, 483, 4140
- Rubin, K. H. R., Diamond-Stanic, A. M., Coil, A. L., Crighton, N. H. M., & Moustakas, J. 2018, *ApJ*, 853, 95
- Sahu, K. 2021, WFC3 Data Handbook, Version 5.0 (Baltimore, MD: Space Telescope Science Institute)
- Salzer, J. J., Jangren, A., Gronwall, C., et al. 2005, *AJ*, 130, 2584
- Salzer, J. J., Gronwall, C., Lipovetsky, V. A., et al. 2000, *AJ*, 120, 80
- Schmidt, K. B., Treu, T., Brammer, G. B., et al. 2014, *ApJL*, 782, L36
- Schneider, D. P., Schmidt, M., & Gunn, J. E. 1999, *AJ*, 117, 40
- Sersic, J. L. 1968, *Atlas de Galaxias Australes* (Córdoba: Observatorio Astronómico de Córdoba)
- Siebenmorgen, R., Carraro, G., Valenti, E., et al. 2011, *Msngr*, 144, 9

- Simons, R. C., Papovich, C., Momcheva, I., et al. 2021, *ApJ*, **923**, 203
- Smith, M. G. 1975, *ApJ*, **202**, 591
- Snyder, G. F., Torrey, P., Lotz, J. M., et al. 2015, *MNRAS*, **454**, 1886
- Somerville, R. S., & Dave, R. 2015, *ARA&A*, **53**, 51
- Steidel, C. C., Erb, D. K., Shapley, A. E., et al. 2010, *ApJ*, **717**, 289
- Stott, J. P., Bielby, R. M., Cullen, F., et al. 2020, *MNRAS*, **497**, 3083
- Struder, L., Briel, U., Dennerl, K., et al. 2001, *A&A*, **365**, L18
- Tumlinson, J., Peebles, M. S., & Werk, J. K. 2017, *ARA&A*, **55**, 389
- Turner, M. L., Schaye, J., Steidel, C. C., Rudie, G. C., & Strom, A. L. 2014, *MNRAS*, **445**, 794
- Turner-Valle, J. A., Sullivan, J., Mentzell, J. E., & Woodruff, R. A. 2004, *Proc. SPIE*, **5487**, 317
- van Dokkum, P. G. 2001, *PASP*, **113**, 1420
- Van Rossum, G., & Drake, F. L. 2009, Python 3 Reference Manual (Scotts Valley, CA: CreateSpace)
- Virtanen, P., Gommers, R., Oliphant, T. E., et al. 2020a, *NatMe*, **17**, 261
- Virtanen, P., Gommers, R., Burovski, E., et al. 2020b, scipy/scipy: SciPy v1.5.2, Zenodo, doi:[10.5281/zenodo.3958354](https://doi.org/10.5281/zenodo.3958354)
- Wooten, A., & Thompson, A. R. 2009, *IEEEP*, **97**, 1463
- Zabl, J., Bouche, N. F., Wisotzki, L., et al. 2021, *MNRAS*, **507**, 4294